Experimental reality of geostrophic adjustment

A. Stegner,
Laboratoire de Météorologie Dynamique, CNRS,
ENS, 24, rue Lhomond, 75231 Paris Cedex 05, France.

September 22, 2006

1 The Holy Graal of rotating shallow-water flows

The rotating shallow water model (RSW) is probably the most pedagogical and useful model to understand geophysical fluid dynamics. Even if the RSW equations are based on drastic assumptions (hydrostatic balance, quasi-bidimensionality, weak dissipation) it is a surprisingly good model of many phenomena in the atmosphere and the ocean. Nevertheless, as far as laboratory experiments are concerned, one should keep in mind that the dynamics of a rotating and stratified fluid is given by the full three-dimensional Navier-Stokes equations at the final place. As it was shown in the chapter 1, the RSW equations can be derived from the primitive equations according to an asymptotic expansion which indeed remains valid for some restricted range of dynamical parameters. However, this derivation starts from the hydrostatic and non-dissipative primitive equations (chapter 1), while both hydrostatic and dissipative effects could play a role in the laboratory. Hence, we recall in this Section the derivation of the RSW model from the Navier-Stokes equations. The main purpose is to understand here which dynamical processes are filtered out by the RSW model while they occur sometimes in real experiment. Moreover, we will try to specify the value of the dynamical parameters needed to be achieve in laboratory experiments in order to be close to the RSW dynamics.

1.1 Single layer f-plane configuration

Let us consider first a single barotropic and incompressible fluid layer in a rotating tank with a flat bottom and a free upper surface, as shown figure 1.

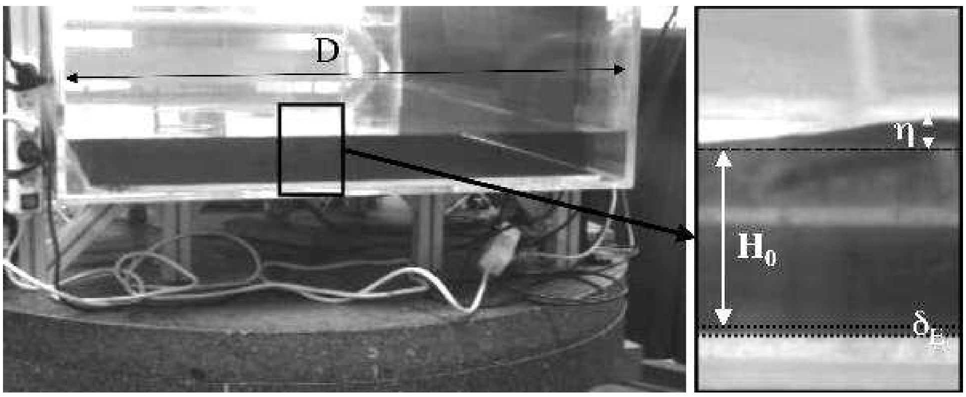

FIGURE 1 Single water layer on a rotating turntable $H_0 = 10cm$ and $D = 90cm$.

In order to get a dimensionless set of equations we use: L and H_0 as horizontal and vertical scales, T the characteristic time-scale for the flow evolution, U and $U(H_0/L)$ as horizontal and vertical velocity scales, $\rho g H_0$ as the charcteristic hydrostatic pressure scale and $\rho f U L$ the scale of pressure deviation from hydrostatic balance ($f = 2\Omega_0$ the Coriolis parameter). Using this dimensionless formulation, the Naviers-Stokes equations can be written as follows:

$$\varepsilon \partial_t u + Ro\mathcal{D}u - v = -\partial_x \pi + E_k \Delta u \tag{1}$$

$$\varepsilon \partial_t v + Ro\mathcal{D}v + u = -\partial_y \pi + E_k \Delta v \tag{2}$$

$$\alpha^2 \left[\varepsilon \partial_t w + Ro\mathcal{D}w\right] = -\partial_z \pi + \alpha^2 E_k \Delta w \tag{3}$$

where $\mathcal{D} = u\partial_x + v\partial_y + w\partial_z$ and $\Delta = \partial_{z^2} + \alpha^2(\partial_{x^2} + \partial_{y^2})$. Besides, in this formulation we decouple the hydrostatic pressure P_H corresponding to the fluid at rest and the dynamical pressure π (pressure deviation induced by the fluid motion) according to:

$$P = P_H(z) + \frac{Ro}{Bu}\pi(x, y, z, t) \tag{4}$$

where $P_H(z) = 1 - z + P_0$ and P_0 is the dimensionless pressure at the free-surface.

In addition one should consider the continuity equation

$$\partial_x u + \partial_y v + \partial_z w = 0 \tag{5}$$

with upper ($z_1 = 1 + \lambda\eta$) and lower ($z_0 = 0$) boundary conditions:

$$u(z_0) = v(z_0) = w(z_0) = 0 \tag{6}$$

$$Row(z_1) = \lambda \left[\varepsilon \partial_t \eta + Ro\left(u\partial_x \eta + v\partial_y \eta\right)\right] \tag{7}$$

$$\pi(x, y, z_1, t) = \frac{\lambda Bu}{Ro}\eta(x, y, t) \tag{8}$$

where $\eta(x, y, t)$ is the dimensionless deviation of the free-surface.

We have introduced in this formulation the following non-dimensional parameters:

- The **Ekman number** $E_k = \frac{\nu}{fH^2}$ fix the vertical scale $\delta_E = \sqrt{E_k}H_0 = \sqrt{\nu/f}$ of the viscous Ekman layer, where ν is the fluid viscosity. According to the standard boundary layer theory, this viscous layer cannot be neglected at the bottom boundary where the no-slip condition (6) must be satified (Gill, 1982; Pedlosky, 1987; Vallis, 2006). In the laboratory, the thickness of this boundary layer is fixed only by the rotation rate $\Omega_0 = 2\pi/T_0$. For typical values of $\Omega_0 \simeq 1 - 10\,rpm$ we get $\delta_E \simeq 1 - 2mm$. Hence, as far as $H_0 \gg \delta_E$, we usually neglect viscous effects in the upper part of the fluid layer ($z \geq 2 - 3\delta_E$). Nevertheless, the Ekman layer forces a secondary re-circulation which induces an efficient transfert of angular momentum from the boundary to the whole fluid domain (Greenspan, 1968). For a fluid layer close to the geostrophic balance the characteristic decay time of this Ekman pumping is $T_E = H_0/\sqrt{\nu f} = T_0/(4\pi\sqrt{E_k})$ (Pedlosky, 1987). Therefore, if we want to neglect this dissipative process over at least several rotation period T_0, the Ekman number should be quite small $E_k \leq 10^{-4}$. Such values can be easily reached if the fluid layer is thick enough.

- The **aspect ratio parameter** $\alpha = H_0/L$. While this parameter is generally small for synoptic atmospheric or oceanic structures ($\alpha \simeq 10^{-2} - 10^{-3}$), this is not always the case in laboratory experiments. Indeed, we could hardly work with ultra-thin layers. The first limitation is due to the surface tension which acts on a millimeter scale. The second constraint is due to the Ekman pumping described above. Hence, typical layer depths in rotating tank experiments are about few tens of centimeters $H_0 \simeq 10-50\,cm$. Therefore, in order to get a small aspect ratio (at least $\alpha \simeq 0.1$) the characteristic horizontal scales should be about $L \simeq 1-5m$. To study the dynamics of multiple structures or to avoid the end effects, the experiment should then be done on a very large turntable $D \simeq 10m$. A unique installation reaches such large scale ($D = 13m$), the Coriolis turntable[1] in Grenoble, France. However, for medium size experiments ($D \simeq 1-2m$) the aspect ratio parameter cannot be asymptotically small and is often close to unity $\alpha \simeq 1$.

- The classical **Rossby number** $Ro = \frac{U}{fL}$ characterizes the importance of rotation in the fluid layer. In order to be consistent, the horizontal scale L in the Rossby number Ro should correspond to the characteristic scale of the horizontal velocity gradient. In other words, the Rossby number quantifies the ratio of the relative vorticity $\zeta = \partial_x v - \partial_y u$ with respect to the planetary vorticity ($Ro \simeq \zeta/f$). For large-scale flows, the Rossby number is generally small or finite in the atmosphere and the ocean, leading to the geostrophic balance. It will exceed unity only for very intense vortices, such as hurricanes. This parameter is usually well controlled in a rotating experiment and both small and large values could be obtained. Nevertheless, to reach large value which would exceed unity an external forcing is generally needed. Indeed, without external energy source, from any initial state the geostrophic adjustment process will quickly lead to a mean flow in geostrophic balance which implies small or finite Rossby numbers ($Ro \leq 1$).

- We introduce here the **time evolution parameter** $\epsilon = \frac{1}{fT}$. This parameter quantifies the dynamical evolution of the flow. It depends on the flow response to the initial condition or to the external forcing. Hence, this parameter cannot be fixed by the experimental setup. Classical textbooks (Gill, 1982; Pedlosky, 1987) usually consider the case of large-scale and slow advective motion and therefore the time-evolution parameter and the Rossby number are fixed to be of the same order $\varepsilon \simeq Ro$. However, for high frequency linear waves (i.e. short gravity-waves) $\varepsilon \geq 1$ and $Ro \ll 1$ while for intense cyclones $Ro \geq 1$ and $\varepsilon \ll 1$. Hence, as far as experiments on geostrophic adjustment are concerned, it is useful to consider both the cases of slow ($\varepsilon \ll 1$) advective motion or fast ($\varepsilon \geq 1$) wave motion independantly of the Rossby number value.

- The **Burger number** $Bu = (R_d/L)^2$where $R_d = \sqrt{gH_0}/f$ is the Rossby deformation radius. As far as we consider a relatively thick layer $H_0 \simeq 10-50\,cm$ and a relatively slow rotation rate $\Omega_0 \simeq 1-10\,rpm$ we get a large deformation radius $R_d \geq 50cm$ which is usually close to the size of the experimental apparatus. Hence, with a single barotropic layer, we can hardly obtain small Burger number values. Only few experiments using high rotation speed ($\Omega_0 \simeq 60\,rpm$) reached small Burger number value within a single layer configuration. However, in such case a parabolic vessel is needed to compensate the resulting parabolic shape of the free-surface (Nezlin and Snezhkin, 1993; Stegner and Zeitlin, 1998; von de Konijnenberg *et al.*, 1999). For such setups the strong curvature of the fluid layer induces, as in the spherical planetary geometry, a strong beta effect. Hence, such parabolic configurations are relevent to model large-scale planetary flows, as the Jovian atmosphere for instance.

- The **relative elevation parameter** $\lambda = \eta_0/H_0$ where η_0 is the characteristic amplitude of the free surface deviation. When the flow is close to geostrophic balance, namely when the dynamical pressure gardient $\nabla\pi$ is balanced at the same order by the Coriolis force, the relative geopotential deviation λ depends on both the Rossby and the Burger number $\lambda \sim Ro/Bu$ (cf. Chapters I and II).

[1]http://www.coriolis-legi.org

The RSW model is based on three main approximations: weak dissipation, hydrostatic balance and quasi-bidimensionality of the horizontal velocity. We discuss, in what follows, when and in which range of dynamical parameters these approximations could be valid or not.

We first assume the **hydrostatic balance** for the whole pressure field. The vertical acceleration in (3) could be neglected if both $\alpha^2 Ro \ll 1$ and $\alpha^2 \varepsilon \ll 1$. Note that for rotating flows, the shallow-water constraint ($\alpha \ll 1$) is not necessary to get the hydrostatic balance. Indeed, a weakly viscous ($E_k \ll 1$) slow ($\varepsilon \ll 1$) and geostrophic ($Ro \ll 1$) flow will follow the hydrostatic balance even if the aspect ratio parameter α is finite. Hence, hopefully for the experimentalists, quasi-geostrophic motions can be accuratley reproduced in a rotating tank while $\alpha \simeq 1$. Nevertheless, the shallow-water constraint is not a sufficient condition that guarantees the hydrostatic balance. Indeed, if the system supports high frequency waves ($\varepsilon \gg 1$) they could be a source of non-hydrostatic motion or instability. Besides, the case of intense ($Ro \simeq 1$) shallow-water ($\alpha \ll 1$) vortices or jets is also complex. These intense structures could exhibit in anticyclonic vorticity region an inertial or centrifugal instability which generate three-dimensional and non-hydrostatic perturbations within the large scale flow (Teinturier *et al.*, 2006). Such short-wavelength instabilities could amplify small-scale perturbations (having a finite aspect ratio $\alpha_p \simeq 1$) with a rapid growth rate ($\varepsilon_p \simeq 1$). In such case, the cyclonic vorticity regions may satisfy the hydrostatic balance, while intense non-hydrostatic motion occurs in the anticyclonic regions (cf. figure 5 below).

However, when the evolution of a shallow-water flow (or its unstable perturbations) is not fast ($\varepsilon \leq 1$) the hydrostatic balance is satisfied at the first order of approximation and equation (3) leads to:

$$\partial_z \pi = 0 \tag{9}$$

Then according to (8) the dynamical pressure becomes directly proportional to the free-surface geopotential deviation:

$$\pi(x, y, t) = \eta(x, y, t) \tag{10}$$

We then assume that the fluid layer experiences a **weak dissipation**. The viscous terms in equations (1-2) could be neglected at a first order of approximation if the Ekman number is small enough $E_k \ll 1$. However, we cannot totally suppress the no-slip condition at the bottom and we should introduce an Ekman layer. This layer will then change the bottom boundary conditions for the upper inviscid layer. It will allow a free-slip condition for the horizontal velocities $(u(z_0), v(z_0))$ but will induce a non-zero vertical velocity. In the case of hydrostatic and slow geostrophic motions this vertical velocity is proportional to the horizontal flow vorticity (Pedlosky, 1987; Vallis, 2006) and the boundary conditions (6) should be replaced by:

$$w(z_0) = \sqrt{\frac{E_k}{2}}(\partial_x v - \partial_y u) = \sqrt{\frac{E_k}{2}}\zeta \tag{11}$$

where ζ is the vertical component of vorticity. Hence, the horizontal dissipation and the Ekman pumping mechanism could be neglected if $\sqrt{E_k} \ll 1$. Practically, in laboratory experiments the dissipation will be a second order process when $E_k \leq 10^{-4}$ at least.

The third approximation assume a **quasi-bidimensional horizontal flow**, in other words, the vertical derivatives $\partial_z u$ and $\partial_z v$ are expected to be negligible. This assumption corresponds to the Taylor-Proudman theorem which is valid only in the limit of small Rossby number (geostrophic flows). A similar approximation is made by the closure hypothesis (22) given in the introduction, which decorrelate the vertical averaging of the horizontal velocity field. Then integrating the continuity equation (22) along the vertical and using the boudary conditions (7) and (11) we finally obtain the following dimensionless formulation of the RSW model :

$$\varepsilon \partial_t u + Ro \mathcal{D}_h u - v = -\partial_x \eta \tag{12}$$

$$\varepsilon\partial_t v + Ro\mathcal{D}_h v + u = -\partial_y \eta \tag{13}$$

$$\lambda\left[\varepsilon\partial_t \eta + Ro\mathcal{D}_h \eta\right] + (1+\lambda\eta)\, Ro\left[\partial_x u + \partial_y v\right] = Ro\sqrt{\frac{E_k}{2}}\zeta \tag{14}$$

where $\mathcal{D}_h = u\partial_x + v\partial_y$ and $\zeta = \partial_x v - \partial_y u$.

Strictly speaking, these RSW equations are valid in the asymptotic limit of slow quasi-geostrophic flows even if the aspect ratio parameter is finite $\alpha \simeq 1$. However, this model is often accurate beyond its limit of validity for finite Rossby number ($E_k \ll 1;\ \varepsilon \ll 1;\ Ro \leq 1$) and could be applied to a wide variety of laboratory experiments. This will be indeed the case if the vertical motions remain weak enough ($w \ll 1$). This latter condition implies both the hydrostatic balance (9) and a quasi-bidimensional horizontal flow. Nevertheless, in such case, high-order terms should be added in (11) to account for non-linear Ekman pumping (Sanson and van Heijst, 2000; Hart, 2001).

1.2 Influences of the centrifugal force

Since the Newton's bucket experiment (1689) it is well known that the free-surface of a fluid layer in solid body rotation is deformed under the action of the centrifugal force. The surfaces of constant pressure for a fluid at rest in the rotating frame (i.e. equipotential surfaces $\Phi = Cst$) are given by the potential function:

$$\Phi(R,\, Z) = -\frac{1}{2}\Omega_0^2 R^2 + gZ \tag{15}$$

Hence, the free-surface of a rotating fluid layer satifies a parabolic shape. Moreover, according to (15), all the equipotential surfaces corresponds to the same paraboloid simply translated along the rotation axis (figure 2(a)). We use in what follows a dimensionless formulation where H_0 is the mean thickness of the layer, D is the tank diameter and $Z_c = g/\Omega_0^2$ is the curvature radius at the center of the parabola. In cylindrical coordinates, the equation for the unperturbed free-surface can be written as :

$$h(r) = \frac{Z}{H_0} = 1 + \frac{1}{2H_0 Z_c}(R^2 - \frac{1}{8}D^2) = 1 + \frac{1}{2}\frac{\beta}{\alpha}(r^2 - \frac{1}{8}d^2) \tag{16}$$

We have introduced here two dimensionless parameters:

- The **dimensionless tank diameter** $d = D/L$. The experimentalist tend to use a large tank $d \gg 1$ in order to satisfy the shallow-water constraint and to avoid the boundary effects. However, for such case, the influence of the centrifugal force could become non negligible close to the wall.

- The **curvature parameter** $\beta = L/Z_c$ quantifies the influence of the curved equipotential surfaces on a dynamical structure of horizontal size L. For the atmosphere or the oceans an equivalent parameter is induced by the spherical geopotential where Z_c is replaced by the earth radius R_E. It is therefore natural to chose a coordinate system so that the unpertubed water surface, or any equipotential surfaces, is given by $z = Cst$. Hence, paraboloidal coordinates should be used for rotating laboratory experiments (Nycander, 1993) while spherical coordinates are used for planetary flows (Pedlosky, 1987). However, for small values of the curvature parameter ($\beta \ll 1$) the tangent plane approximation is generaly made. In other words, a cartesian system of coordinates is used locally and the corrective terms induced by the parabolic curvature will appear only at the order $\beta^2 d$ (Nycander, 1993; Stegner and Zeitlin, 1995). If we consider a medium scale experiment ($D \simeq 100cm$) and a typical horizontal scale $L \simeq 10cm$, these corrective terms could be neglected for moderate rotation rate ($\Omega_0 \leq 10rpm$).

The main difference between rotating laboratory experiments and planetary flows is that the effective gravity g^e is variable in both direction and amplitude in the laboratory. Indeed, when the centrifugal force is not negligible, it induces a tilting of the effective gravity but also a change in its amplitude (figure 2(a)). The latitudinal dependence of the effective gravity (also called the γ-effect) in paraboloidal coordinates and in the tangent plane approximation is given by:

$$\frac{g^e}{g} = \frac{1}{cos\theta} = \sqrt{1+\beta^2 r^2} \simeq 1 + \frac{1}{2}\beta^2 r^2 \tag{17}$$

For paraboloidal equipotential surfaces this latitudinal dependance of the effective gravity is of the same order than the latitudinal dependance of the Coriolis force (classical β-effect).

$$\frac{f}{f_0} = \frac{\Omega_z}{\Omega_0} = cos\theta \simeq 1 - \frac{1}{2}\beta^2 r^2 \tag{18}$$

Under the tangent plane approximation the equipotential surface are assumed to be locally flat (figure 2(b)) while the radial variations of the effective gravity g^e, the local component of rotation Ω_z and the unperturbed layer depth h are expended at the first order in $y = r - a$ the local latitudinal coordinate centered at the radial position $r \simeq a$.

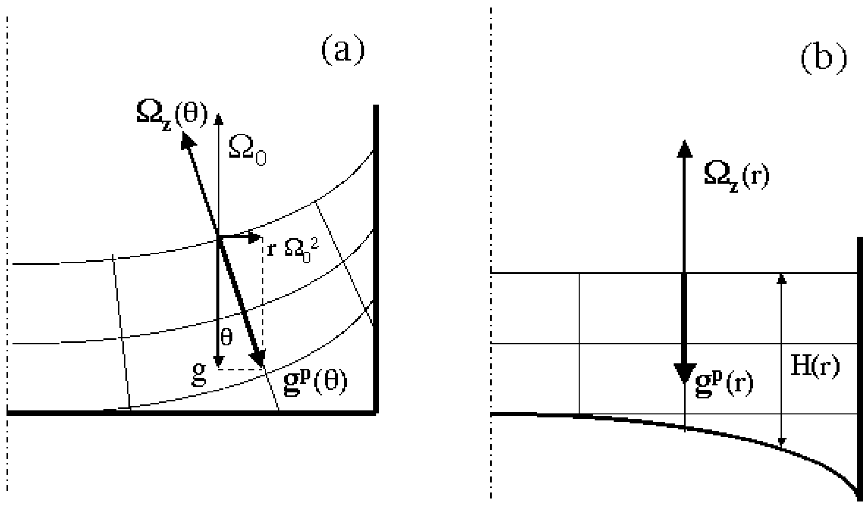

FIGURE 2 Parabolic deformation of the equipotential surfaces (thin lines) due to the centrifugal acceleration in rotating laboratory experiments (a). Schematic description of the tangent plane approximation when the corrective terms of order $\beta^2 d$ could be neglected (b).

If we consider the center of the rotating tank ($a = 0$ and $y = r$), according to (16-18) the latitudinal variations of $h(y)$, $\Omega_z(y)$ or $g^e(y)$ are all quadratic and when $\beta/\alpha = L^2/(Z_c H_0) \ll 1$ the fluid layer respect the f-plane configuration at the first order of approximation. This will be generally the case for moderate rotation rate ($\Omega_0 \leq 10rpm$) in a central region of few tens of centimeter ($r \leq 10 - 20cm$). However, out from the center, the latitudinal variations could be linearly expended in y and they reach their extremal values at the tank wall. Therefore, in order to quantify the relative influence of the β-effect, the γ-effect or the topography, we estimate (when $a = d$) the magnitude of the following first derivatives : $\partial_y h/h \propto \beta d/\alpha$, $\partial_y f/f \propto \beta^2 d$ and $\partial_y g^e/g^e \propto \beta^2 d$. Hence, for standard experimental configuration ($\beta \ll 1$, $\alpha \leq 1$, $d \gg 1$) the y-dependence of the equilibrium layer depth induces by the parabolic free-surface deformation is the dominant effect. Due to this topographic effect, the equilibrium fluid layer can support topographic-Rossby waves. The linear dispersion relation of these low-frequency waves is analogous to planetary Rossby waves and they are strongly coupled with the slow geostrophic motion. This effect may induces, for instance, a significant drift velocity ($V_d \simeq fL(\partial_y h/h)$ when $L \leq R_d$) and the dispersion of localized vortices (Matsuda *et al.*, 1990; Carnevale *et al.*, 1991; Flor and Eames, 2002). Hence, the dynamical influence of the topographic variations could be neglected in the whole tank, from the center to the wall, if $\partial_y h/h \propto \beta d/\alpha \ll \varepsilon$. The latter criterion will be generally satisfied in a medium scale experiment ($D \simeq 100cm$) if the rotation rate is weak enough ($\Omega_0 \leq 4rpm$).

However, if the ratio $\beta d/\alpha$ become too large, the variation of the layer thickness induced by the centrifugal force could be compensated with a parabolic bottom topography or a parabolic vessel adjusted to the rotation rate (Nezlin and Snezhkin, 1993; Stegner and Zeitlin, 1998; von de Konijnenberg *et al.*, 1999).

1.3 Non-hydrostatic wave modes

Focusing on the geostrophic adjustment problem, where both slow geostrophic motion and fast waves are generated, we look here more carfully at the wave motion that may occurs in a rotating fluid layer. We linearize the primitives equations (1-8) assuming small amplitudes for the velocity $Ro \ll 1$ and the free surface displacement $\lambda \ll 1$. We neglect all dissipative terms ($E_k \ll 1$) and take the deformation radius as a characteristic horizontal scale $L = R_d$ of the unperturbed rotating fluid layer, therefore $Bu = 1$ and $\alpha = H_0/R_d$. Besides, we keep in mind that the aspect ratio α cannot be asymptotically small for laboratory experiment and we keep the vertical acceleration in (3). Hence, we get :

$$\varepsilon\partial_t u - v = -\partial_x \pi \tag{19}$$

$$\varepsilon\partial_t v + u = -\partial_y \pi \tag{20}$$

$$\alpha^2\varepsilon\partial_t w = -\partial_z \pi \tag{21}$$

$$\partial_x u + \partial_y v + \partial_z w = 0 \tag{22}$$

with upper ($z_1 = 1$) and lower ($z_0 = 0$) boundary conditions

$$w(z_0) = 0 \tag{23}$$

$$w(z_1) = \varepsilon\partial_t \eta \tag{24}$$

$$\pi(z_1) = \eta \tag{25}$$

According to the space and time shift invariance of the system, we use the following Fourier decomposition $A(x, y, z, t) = A_0(z)\, e^{i(t-kx-ly)}$ for all variables. In this case the temporal evolution parameter corresponds to a dimensionless wave frequency $\varepsilon = \widetilde{\omega}/f$. This linear system finally leads to:

$$\partial_{z^2}\pi_0 + \frac{\alpha^2\varepsilon^2 K^2}{1-\varepsilon^2}\pi_0 = 0 \tag{26}$$

where $K^2 = k^2 + l^2$, with the boundary conditions

$$\partial_z \pi_0(0) = 0 \tag{27}$$

$$\partial_z \pi_0(1) = \alpha^2\varepsilon^2\pi_0(1) \tag{28}$$

For **inertia-gravity waves** ($\varepsilon > 1$) we obtain the following dispersion relation:

$$\gamma\, tanh(\gamma) = \alpha^2\varepsilon^2 \; ; \; \gamma^2 = \frac{\alpha^2\varepsilon^2 K^2}{\varepsilon^2 - 1} \tag{29}$$

We can see here that we will recover the dispersion relation of Poincaré waves

$$\varepsilon^2 = 1 + K^2 \tag{30}$$

only if $\alpha K \ll 1$, in such case short inertia-gravity waves are dispersionless. This condition is more restrictive than the shallow-water constraint $\alpha \ll 1$, and indeed short enough gravity waves will always deviate from the RSW model. We have plotted in figure 3 the deviation from the Poincarré dispersion relation for various values of the aspect ratio parameter α that could be found in laboratory experiment.

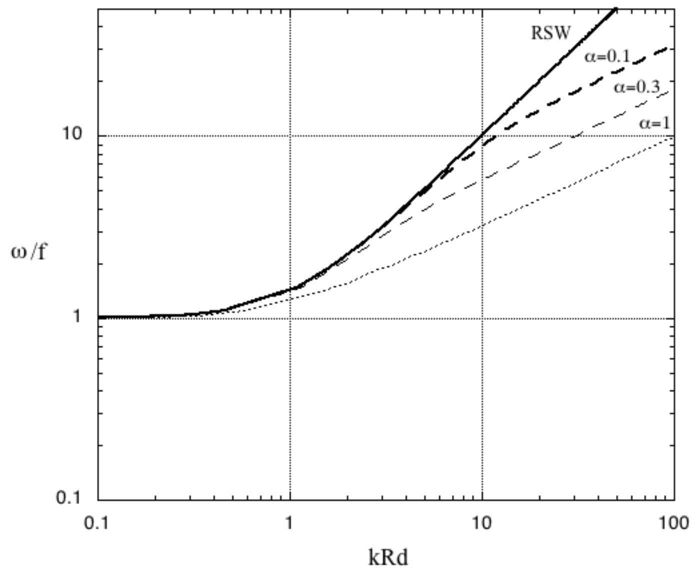

FIGURE 3 Log-log plot of the dimensionless dispersion relation for inertia-gravity waves. The curves correspond to diferent values of the aspect ratio parameter: RSW model, or $\alpha = 0$ (thick line), $\alpha = 0.1$ (thick dashed line), $\alpha = 0.3$ (thin dashed line), $\alpha = 1$ (thin dotted line).

For a finite value of the aspect ratio parameter, $\alpha = 0.3$ for instance as it is shown in figure 4, high-frequency waves ($\varepsilon \gg 1$) or in other words short-waves ($K \gg 1$) will satisfy the dispersion relation of non-rotating surface gravity waves (SGW).

$$\varepsilon^2 = \frac{K}{\alpha} tanh(\alpha K) \tag{31}$$

It can be shown that the same dispersion relation (31) applies for boundary Kelvin waves propagating along a lateral wall of the tank. Hence, unlike the RSW model, both inertia-gravity waves and Kelvin waves will become dispersive in the short-wave limit if the aspect ratio parameter is not small enough. Nevertheless, theses non-hydrostatic effects could be neglected for a wide range of the inertia-gravity wave spectrum if $\alpha K \ll 1$, which corresponds to

$$\widetilde{\lambda} \gg 2\pi H_0 \tag{32}$$

where $\widetilde{\lambda}$ is the characteristic wavelength.

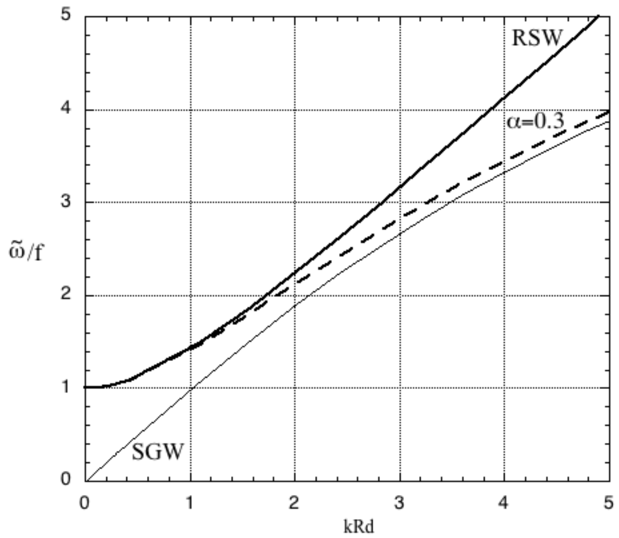

FIGURE 4 Dimensionless dispersion relation of inertia-gravity waves corresponding to the RSW model (thick line), in a non-rotating (thin line) and a rotating fluid layer (thick dashed line) for the fixed value of $\alpha = H_0/R_d = 0.3$.

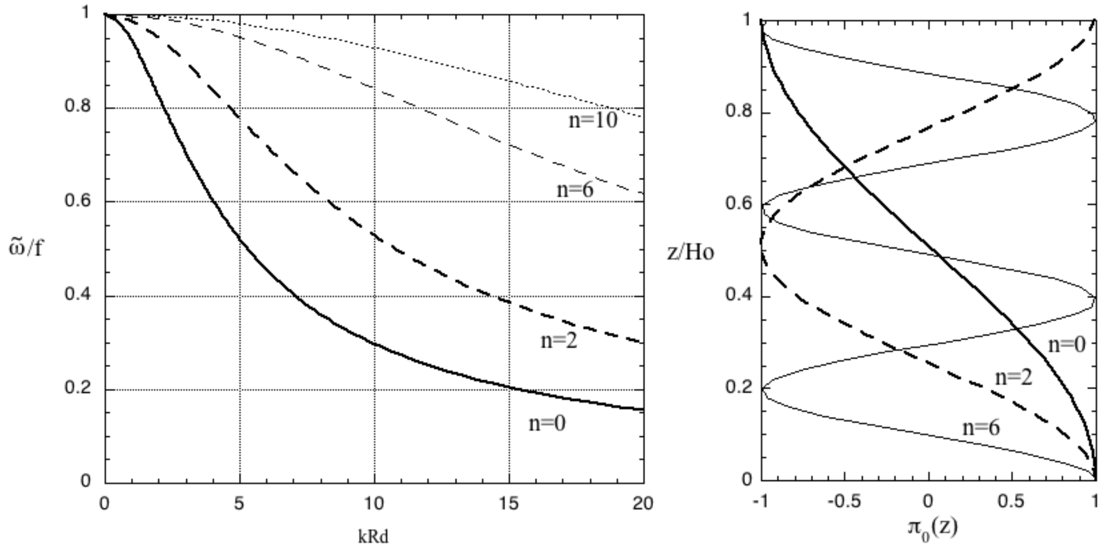

FIGURE 5 Dimensionless dispersion relation of non-hydrostatic inertial waves (left panel) corresponding to various vertical modes (right panel). All these wave modes are calculated for the aspect ratio parameter $\alpha = H_0/R_d = 1$.

For **inertial waves** ($\varepsilon < 1$) we obtain a discrete spectrum of n vertical modes which correspond to the dispersion relations:

$$-\gamma_n tan(\gamma_n) = \alpha^2 \varepsilon_n^2 \; ; \; \gamma_n^2 = \frac{\alpha^2 \varepsilon_n^2 K_n^2}{1 - \varepsilon_n^2} \tag{33}$$

where $(1+n)\pi/2 < \gamma_n < (1+n)\pi$.

These non-hydrostatic waves exhibit strong variations of pressure and velocity along the vertical axis (figure 5 right panel). When the vertical wavenumber becomes large ($n \gg 1$) the wave frequency approches the Coriolis frequency $\varepsilon \simeq 1$ for a wide range of horizontal wavenumber components. According to figure 5 (left panel), for a given horizontal wavelength k, the short wavelength perturbations along the vertical will have the highest horizontal phase speed. Hence, the non-hydrostatic inertial waves play a crucial role in the vertical alignment and the rapid formation of Taylor columns in a rotating fluid layer.

If now we add a mean flow component, such type of non-hydrostatic modes will lead to inertial instability in anticyclonic vorticity regions (Johnson, 1963; Yanase, 1993). Such instabilities occur when the Rossby number Ro exceeds unity and the maximum growth rates for these three- dimensionnal modes are reached when $Ro \simeq 2$. For larger Rossby numbers, the influence of rotation becomes negligible, and the growth rates of such unstable modes are strongly reduced. Hence, for finite Rossby numbers, starting initially from a two-dimensionnal flow the three dimensionnal perturbations could growth exponentially and break both the hydrostatic and the geostrophic balance (Afanasyev and Peltier, 1998; Stegner *et al.* 2005). As it can be seen in figure 6, such small-scale instability may occurs in shallow-water anticyclonic vortices when the Rossby number is large enough.

FIGURE 6 Dye vizualisation of von Karman wake in a rotating shallow-water layer with $\alpha \simeq 0.07$, $Ro \simeq 2$ and $Re \simeq 20000$. Small-scale instability is visible in anticyclonic vortices (black dye), while cyclonic vortices (red dye) remain stable (Teinturier *et al.*, 2006)

1.4 Two-layer stratification

We have seen previously that with a single barotropic layer experiment the deformation radius is generally close to the tank size. In other words, for a single layer f-plane experiment we are restricted to large Burger number dynamics. Nevertheless, if we use a two-layer stratification we introduce a baroclinic deformation radius which could be much smaller than the barotropic one. Besides, the Ekman pumping affects only the lower layer, and for an appropriate set of parameters the upper layer dissipation could be strongly reduced.

To create a density stratification in water, salt or sugar are generally used instead of temperature. Indeed, the thermal diffusivity ($\kappa_T \simeq 10^{-7} m^2.s^{-1}$) is a hundred time larger than the salt diffusivity ($\kappa_S \simeq 10^{-9} m^2.s^{-1}$). In a motionless fluid layer, an initial salt perturbation will diffuse over a 1 cm distance in half a day instead of ten minutes for a thermal perturbation. Hence, for typical layers depth about few to tens of centimeters an initial salt or sugar stratification will remain robust for at least several hours. To obtain a sharp density jump corresponding to a well-defined two-layer stratification we generally proceed as follows. The tank is first filled with the deep and dense lower layer. Then, we start to spin up the rotating table and when the solid-rotation rotation is reached we slowly inject the light upper layer ρ_1 at the surface of the dense bottom layer ρ_2. To reduce the vertical mixing during the injection we could use flotating Hele-shaw cells or small tubes to inject the light fluid horizontally at the free-surface. An other method consists to inject very slowly the upper layer through floating porous plates.

Let us consider a two-layer salt stratification, as shown in figure. According to the classical dimensional analysis we add to the previous ones at least four new dimensionless parameters:

- The **thickness ratio parameter** $\delta = H_1/(H_1 + H_2)$. This parameter controls the dynamical interaction between the two layers. For equivalent depth layers $\delta \simeq 0.5$ the two layers are strongly coupled and baroclinic instability may occurs even if the vertical velocity shear is weak. On the other hand, according to the standard two-layer Phillips model (Pedlosky, 1987), for small ratios $\delta \ll 1$, the baroclinic growth rates tend to vanish. Hence, to avoid a strong baroclinic destabilisation of the flow, we will first consider laboratory experiments with a thin upper layer and a deep lower layer having $\delta \simeq 0.1$. Besides, in order to keep the Ekman number small enough in the lower layer ($E_k^{(2)} = (\delta_E/H_2)^2 \leq 10^{-4} E_k$), we generally fix $H_2 = 10 - 20cm$, and therefore the upper layer thickness is about $H_1 \simeq 2cm$.

- The **density ratio parameter** $N = 2(\rho_2 - \rho_1)/(\rho_2 + \rho_1)$. With salt stratification, we can easily obtain a N small up to 10^{-3}. We then introduce the reduced gravity $g' = Ng \ll g$ which controls the dynamics of internal gravity waves at interface between the layers.

- The **internal Burger number** $Bu' = (R_d'/L)^2$ corresponding to the baroclinic deformation radius $R_d' = \sqrt{g' H_1 H_2 (H_1 + H_2)}/f$. We can see here that for small $N \simeq 10^{-3}$ and $\delta \simeq 0.1$ the baroclinic deformation radius could be two orders of magnitude smaller than the barotropic deformation radius $R_d' \simeq \sqrt{g' H_1}/f \simeq 10^{-2} R_d$, where $R_d = \sqrt{g(H_1 + H_2)}/f$. Hence, for a thin upper layer with $H_1 \simeq 2cm$ and a weak density difference $\rho_2 - \rho_1 \simeq 2 - 10 g.l^{-1}$ we can reach deformation radius as small as $R_d' \simeq 1cm$. Therefore, with a two-layer stratification, the internal Burger number could be easily varied from small to large values $0.01 \leq Bu' \leq 100$.

- We introduce the **stratification parameter** $E_S = (\delta_E/d_S)^2$ in order to quantify the dissipation induced by the fluid-fluid interface. This parameter is an equivalent Ekman number for a continuously stratified fluid where d_S is the characteristic scale of the vertical density gradient. Indeed, for salt stratification, due to the molecular diffusion and the injection process, the density gradient is always continuous between the upper and the lower layer. Even with very slow laminar injection of both layers the characteristic size d_S cannot be infinitely small, and we generally get a density gradient thickness of $d_S = 3 - 5mm$ (Stegner *et al.* 2004). For geostrophic flows, the vertical gradient of the horizontal velocity will be directly proportional to the vertical density gradient. Hence, the dissipative terms in the right-hand side of the horizontal momentum equations (12) should scale with $E_S = (\delta_E/d_S)^2$. This parameter is larger than the Ekman number defined using the upper layer thickness $E_k^{(1)} = (\delta_E/H_1)^2$. However, due to the absence of the no-slip boundary condition, there is no boundary Ekman layer for the upper layer. The fluid-fluid interface will then induce (if any) a much weaker recirculation than a classical bottom Ekman layer if the vertical stratification is not too sharp $E_S = (\delta_E/d_S)^2 \ll 1$.

We get a dimensionless set of equation for the two-layer RSW model with rigid lid and bottom boundary condition using: L as horizontal scale and T the characteristic time-scale for both layers, $U^{(i)}$ as the horizontal velocity, H_i the vertical thickness and $\rho_i f U^{(i)} L$ the pressure deviation from hydrostatic balance in each layer.

$$\varepsilon \partial_t u^{(i)} + Ro^{(i)} \mathcal{D}_h^{(i)} u^{(i)} - v^{(i)} = -\partial_x \pi^{(i)} \tag{34}$$

$$\varepsilon \partial_t v^{(i)} + Ro^{(i)} \mathcal{D}_h^{(i)} v^{(i)} + u^{(i)} = -\partial_y \pi^{(i)} \tag{35}$$

where $\mathcal{D}_h^{(i)} = u^{(i)} \partial_x + v^{(i)} \partial_y$ and the superscrit $i = 1, 2$ corresponds respectively to the upper and the lower layer. The pressure continuity at the interface gives :

$$\frac{\lambda Bu'}{1-\delta} \eta = (1-N) Ro^{(1)} \pi^{(1)} - (1+N) Ro^{(2)} \pi^{(2)} \tag{36}$$

and the mass conservation in each layer leads to:

$$\lambda \left[\varepsilon \partial_t \eta + Ro^{(1)} \mathcal{D}_h^{(1)} \eta \right] + (1 + \lambda \eta)\, Ro^{(1)} \left[\partial_x u^{(1)} + \partial_y v^{(1)} \right] = 0 \tag{37}$$

$$\lambda \delta \left[\varepsilon \partial_t \eta + Ro^{(2)} \mathcal{D}_h^{(2)} \eta \right] - (1 - \delta - \lambda \delta \eta)\, Ro^{(2)} \left[\partial_x u^{(2)} + \partial_y v^{(2)} \right] = (1-\delta)\, Ro^{(2)} \sqrt{\frac{E_k^{(2)}}{2}} \zeta^{(2)} \tag{38}$$

where the relative elevation parameter λ correponds here to the characteristic deviation of the internal interface rescaled by the upper layer thickness H_1.

According to the above equations, if the thickness ratio parameter δ and the density ratio parameter N are small enough and if the motion has a strong baroclinic component (intense velocities in the thin upper layer while the deep lower layer remains almost at rest $Ro^{(2)} \simeq \delta Ro^{(1)}$ (Cushman-Roisin, 1992), the interface deviation η is controlled by the upper layer pressure only $\eta \simeq \pi^{(1)}$. In such case, at the first order of approximation, the upper layer motion is not affected by the lower layer which acts as a neutral layer. Hence, the upper layer dynamics can be described by the shallow-water reduced-gravity model. Namely, a one layer RSW model where the gravity g is replaced by the reduced gravity g' induced by the two-layer stratification.

However, as for the single layer case, non-hydrostatic wave motions or inertial instability may occur in the two-layer experiment when respectively $\widetilde{\lambda} \gg 2\pi H_2$ or $Ro^{(1)} > 1$. Note that the hydrostatic constraint on the wave activity is fixed here by the deep layer thickness H_2 and not the thin upper layer H_1. Recent laboratory experiments performed in a two-layer configuration ($\alpha \simeq 0.66$; $\delta \simeq$0.2) exhibit non-hydrostatic wave behaviour for $\widetilde{\lambda} \simeq 80cm$ wavelength, while $H_1 \simeq 12.5cm$ and $H_2 \simeq 50cm$ (Thivolle-Cazat, 2003).

Taking into acount the above mentioned laboratory constraints, the physical modelling of rotating shallow-water flows looks like a Holy Graal for experimentalist. Nevertheless, for a specific range of the dynamical parameters, the motion in rotating fluid layers could be close to the one layer RSW model. We recall bellow, both for single-layer and the two-layer configurations, the distinct conditions needed to be satisfied, respectively, for the slow vortical motion and the fast wave motion in order to follow the RSW dynamics.

	vortical motion	wave motion
single layer	$\varepsilon\alpha^2 \ll 1$; $Ro\alpha^2 \ll 1$; $Ro < 1$	$kH_0 \ll 1$
two layers	$\delta \ll 1$; $Ro^{(2)} \leq \delta Ro^{(1)}$; $Ro^{(i)}(\alpha^{(i)})^2 \ll 1$; $Ro^{(1)} < 1$	$kH_2 \ll 1$

2 Potential vorticity measurements: a new challenge

Both vorticity and potential vorticity play an important role in the dynamics of rotating fluid layers. The application of the Kelvin theorem to a non-dissipative rotating shallow-water flow implies the Lagrangian conservation of potential vorticity (Chapter 3) in each layer:,

$$\frac{D}{Dt}(\frac{1 + Ro\zeta}{1 + \lambda\eta}) = 0 \tag{39}$$

An elementary fluid parcel (i.e. fluid column) moving within a layer could be stretched or compressed. These changes in the height of the fluid parcel during its motion will be accompanied by a change in its vorticity. In other words, for a purely incompressible two-dimensional flow when the free-surface or the interface deviations are negligible ($\lambda \ll Ro$), we recover the Lagrangian conservation of vorticity:

$$\frac{D\zeta}{Dt} = 0 \tag{40}$$

In this case, vorticity will be generated in the flow only if there is an external source (boundary layer or fluid injection, for instance). For a rotating fluid layer, if the layer thickness varies sufficiently, relative vorticity could be generated from an adjustement process without any external source.

The potential vorticity conservation is a key concept for adjustment processes even in the presence of dissipative forces. Hence, as far as laboratory experiments on geostrophic adjustment are concerned, it is crucial to perform quantitative measurements of the potential vorticity field. Such measurements in a rotating fluid layer are indeed not simple. Both the vorticity field ζ and the height field η should be measured simultaneously. If such measurements are now possible, it is mainly due to recent progress in computers, lasers and cameras technology. Besides, additional difficulties are encountered on a rotating turntable where sufficiently compact devices (especially lasers) and remote control of the whole setup are needed. Therefore, direct measurement of the potential vorticity field is always challenging for experimentalists. We give below some details on the non-intrusive methods which can be used to achieve such measurements for specific experimental configurations.

2.1 Particle image velocimetry and vorticity field measurements

The particle image velocimetry (PIV) was developped since 1994 to perform accurate and quantitative measurements of fluid velocity vectors at a very large number of points simultaneously (Adrian, 2005). Presently, the 2D PIV method consist to add small neutrally buoyant beads to the working fluid and lightened them with a laser sheet. The 2D particle motion along this plane are recorded with a digital video camera. Cross-correlation image processing are then perfomed to measure the mean particle displacement in small box region between two successive images (Fincham, 1997). Standard systems are sold by commercial companies and it is now the most efficent and non-intrusive technique used in fluid mechanics to obtain a vorticity map in a given region of the flow field. Nevertheless, some technical limitation appears which restrict the spatial resolution of such measurements in rotating fluid layers.

The energy necessary to illuminate fine particles and produce images of sufficient exposure and clarity is the first limitation of PIV. The maximum size of the measurement window is then fixed by the laser intensity and the camera exposure time. Hopefully, vertical motion are strongly damped in a rotating fluid layer, therefore neutrally buoyant particles could stay for a relatively long time in a fixed horizontal plane lightened by the laser sheet. Besides, the horizontal velocities of geostrophic motions are usually not too large ($V \simeq 1 - 10cm.s^{-1}$) and the camera exposure time could be optimized to $10-20ms$. But nevertheless, if the intensity per unit area is too small the clarity of recorded images may not be sufficient enough with classical digital camera. On a medium size turntable ($D \simeq 1m$), high power lasers which require cooling systems are generally excluded. However, the last generation of compact high power laser diodes[2] can generate an uniform intensity line (non-gaussian) with an output power up to 1W. With such system we could easily detect the horizontal particle motion ($V < 10cm.s^{-1}$) from small ($10cm \times 10cm$) to large ($1m \times 1m$) areas of investigation.

The second limitation is induced by the pixel resolution of the camera. Indeed, to obtain a precise cross-correlation between two interrogation windows, a minimum number of particles ($\sim 3-5$) should be present in the interrogation box. This constraint induces generally a minimum size of a 8×8 pixel box. Hence, with a standard 750×550 pixels camera we usually get a velocity field of 95×70 vectors as it is shown in figure 8. Using digital cameras with higher resolution (3000×2000 pixels) we could, for instance, reach a 370×250 vector grid field. However, even with very high resolution camera and optimized software, PIV measurements will always give a coarse grid resolution in comparison to direct dye tracer visualizations (3000×2000 pixels) or high-resolution numerical simulations (4096×4096 for two dimensionnal flows (Bracco *et al.* 2000)).

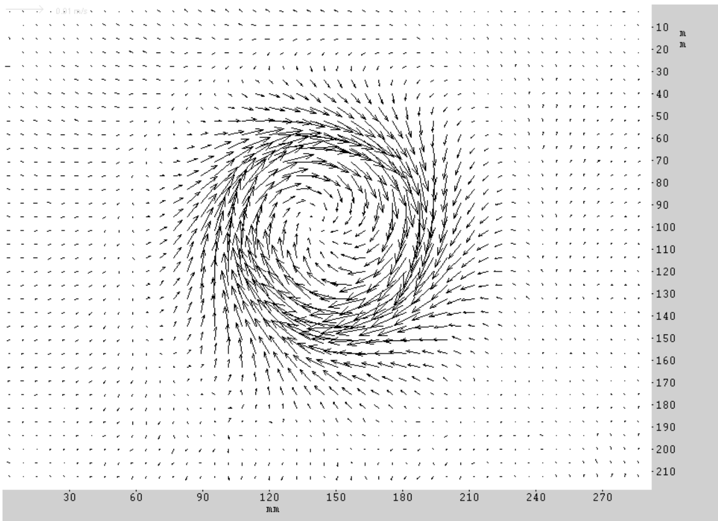

FIGURE 7 Horizontal velocity field of a cyclone obtained from particle image velocimetry. For clarity, only half of the vectors (47×35) are displayed instead of the full (94×70) field. The measurement was made in the thin upper layer of a two-layer stratified fluid corresponding to: $Bu \simeq 0.4$, $\lambda \simeq 0.5$, $\alpha \simeq 0.75$, $\delta \simeq 0.1$.

The third limitation comes from the limited precision of the velocity field. Even with hierarchical correlation methods, where correlations deduced from a large interrogation box are used to guide correlation analysis at smaller boxes (Hart, 2000), the available dynamical velocity range is about 100:1. In other words, the method cannot detect fluctuations in the velocity field below 1%. Besides, experimental noise on recorded images could easily produces 5% error in the velocity field. This can be a serious problem, because a weak noise in the velocity field induces a stronger noise in the derivatives and therefore strongly influences the vorticity measurement. Typical errors of order of 10% (or higher) in the vorticity field could be frequent and strong efforts on the improvement of the image quality and the software used in the PIV process are needed to reach such precision on the vorticity field measurements. However, if the flow evolve slowly in comparison with the frequency of the PIV acquisition system, time averaging of the velocity field is a simple and efficient way to reduce the experimental noise.

[2]Lasiris Magnum Laser (www.laser2000.fr)

For the case of geostrophic adjustment, when a quasi-steady motion is reached, time averaging will lead to sufficiently precise vorticity measurements. For instance, the velocity field shown in figure 8 is an average of ten velocity fields separated by a time interval of $120ms$. Hence, this corresponds to a time averaged velocity measurements over $1.2s$ which is smaller than the inertial period $T_f = 12s$ or the characteristic decay time $T_E = H_2/\sqrt{\nu f} \simeq 200s$. Such time averaging reduces the noise on the vorticity field (figure 8(b)) by a factor 10 in comparision with the instantaneous vorticity measurements (figure 8(a)).

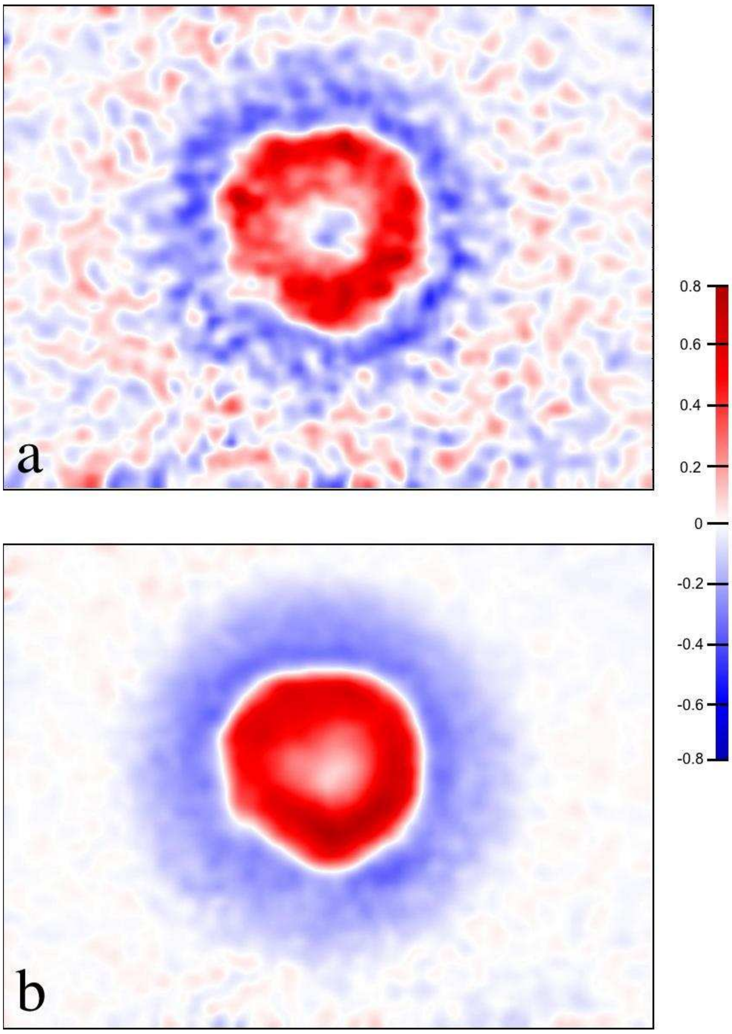

FIGURE 8 Cyclonic (red) and anticyclonic (blue) dimensionless vorticity ζ/f calculated from an instantaneous velocity field (a) or calculated from the time averaged velocity field (b) shown in figure 8. The Rossby number deduced from the maximum vorticity is about $Ro = \zeta_{max}/f \simeq 0.6$. The measurement area is a rectangular window of $280mm \times 220mm$.

According to the above comments, we should emphasize that even if we can easily obtain a vorticity map from the standard PIV system the accuracy of such measurements should be checked carefully. Let us recall, that if PIV measurements have a coarse grid resolution corresponding to 8×8 or 12×12 pixels on the digitized image, this will be even more pronouced for the vorticity field. Indeed, to resolve accurately a gradient, at least $3 - 5$ grid points are needed. Therefore, quantitative vorticity measurements will not be possible if the dynamical structure under consideration is too small. We can roughly estimate a limiting value as 25×25 pixels on the digitized image. Thus, thin vorticity filaments are generally smoothened by the PIV process. In such case it could be usefull to use two cameras with a wide and a zoom angle in order to quantify accurately the large scale flow and smaller vortical structures (Perret *et al.* 2006).

Hence, the standard PIV method is well suited to quantify slow and large-scale structures in rotating fluid layers. However, for fast and small-scale structures such as high-frequency waves, this velocimetry method can hardly provide quantitatives measurements, unless an expensive high-speed PIV technology is used.

2.2 Height field measurements

Laboratory techniques for measuring the velocity field, such as the PIV method described above, are quite advanced. However, methods for making accurate measurements of the height field of a fluid layer have remained relatively elusive. As far as we know, four non-invasive techniques were used to detect or to measure the height field fluctuations in rotating fluid layers: light absorption, optical altimetry from the parabolic free-surface, optical rotation of the working fluid and laser induced visualization (LIV).

Light absorption

The light absorption technique is based on the optical density of a dyed layer. It consists in measuring the light intensity after absorption through a uniformly dyed fluid layer (Holford et al. 1996). The fluid layer is usually lightened from below through a transparent vessel while a video camera records the intensity fluctuations from the top (figure 9(a)). A specific pass-band-filter, which is centered at the maximum absorption of the dye, is put on the video camera to increase the sensitivity. With this method a local increase of the layer thickness induces a higher absorption and this region will appear darker on the video image (figure 9(b)). This altimetric measurements was used succesfully on small-scale parabolic vessel where small (10%) and large (60-100%) relative free-surface deviation were detected with an accuracy of less than one mm (Stegner and Zeitlin, 1998). Nevertheless, caustic effects induce systematic errors of order $5-10\%$ of the layer thickness which limits the precision on the height measurements.

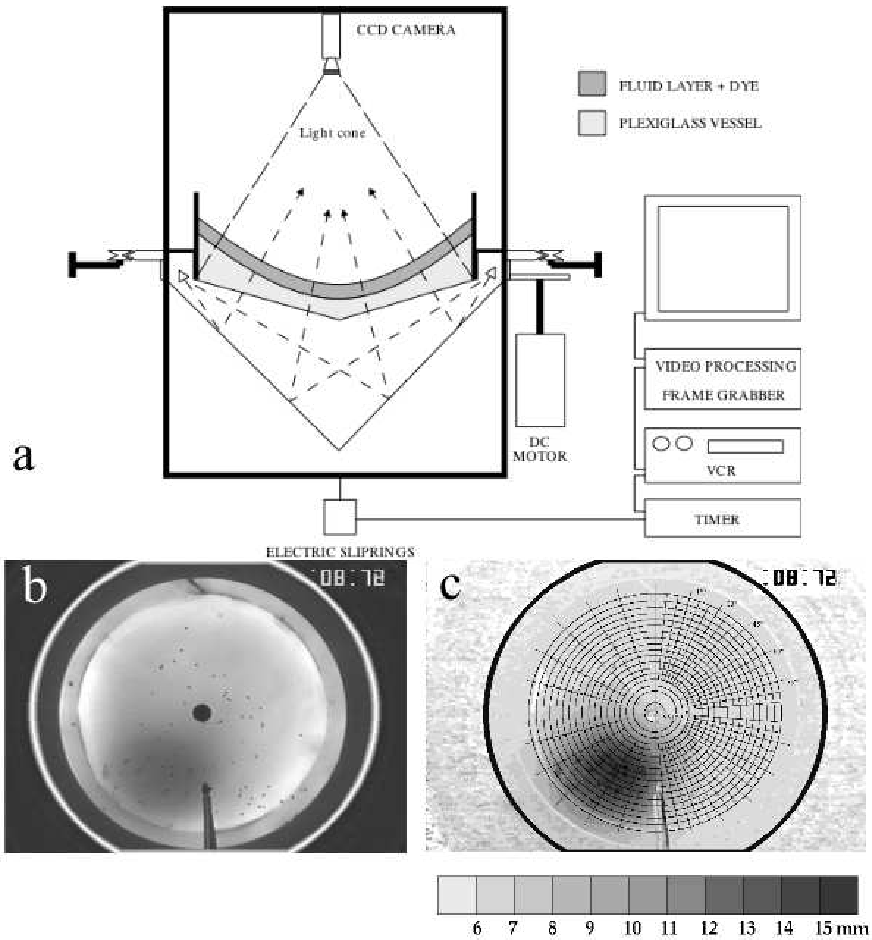

FIGURE 9 Light absorption technique for a parabolic vessel experiment (a) (Stegner and Zeitlin, 1998). Intensity fluctuations view from the top of the experiment (b) post-processed calibrated image corresponding to a relative elevation $\lambda \simeq 1$ of the layer depth (c).

Optical altimetry of the parabolic free-surface

The free-surface fluctuations of a rotating fluid layer can be imaged and analysed using its parabolic free-surface as a Newtonian telescope mirror. Parallel light rays from a source high above the rotating table reflects from the water surface and converges on the parabolic focus $Z_f = \frac{1}{2}Z_c$ (figure 10(a)). However, parallel light rays can hardly be obtained on a rotating table. The image of a point-light source located at Z_c (the radius of curvature at the center) no longer have sharp focus but converge through a small disk located at the same height Z_c (figure 10(b)). For practical purpose the light source and the camera are symmetrically displayed off the axis. Then, putting a knife-edge barrier in the middle of this singular disk, where all the rays converge, can partially obscure the image giving great sensitivity to slight imperfections of the reflecting surface. This optical altimetry technique is one of the most sensitive method used so far in geophysical fluid dynamics experiments. Indeed it is potentialy able to detect free-surface fluctuations with a one micron precision, independently of the mean thickness of the parabolic layer. Therefore, this method is particulary suited for the investigations of small amplitude waves (less than 0.1% fluctuation) which are often difficult to detect by other methods. For instance, an inertia-gravity wave having an amplitude of $50\mu m$ (0.04% of the mean layer thickness) could be visualized in figure 11. Qualitative observations of a large variety of dynamical features such as gravity waves, inertial waves, Rossby waves and small-scale convection could then be performed (Rhines *et al.*, 2006; Rhines, 2006).

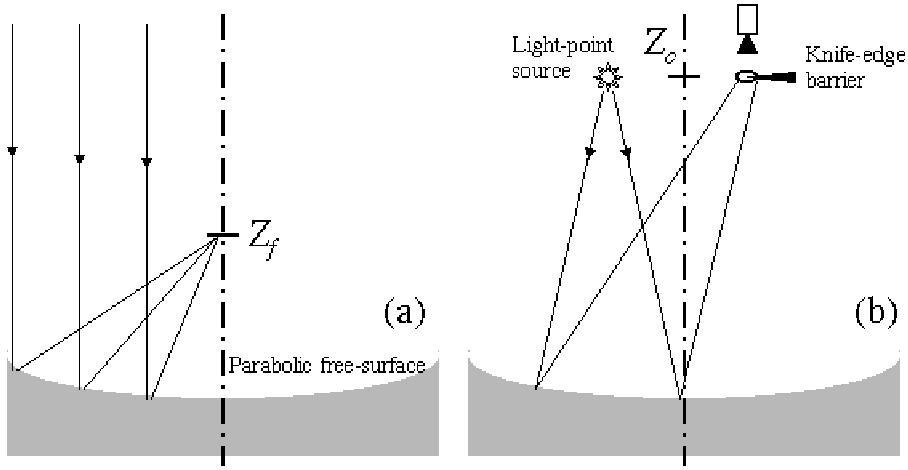

FIGURE 10 Focusing of parallel light-rays reflected by the parabolic free-surface (a). Sharp convergence of a point light-source located close to Z_c the center of curvature of the apex (b). A knife-edge barrier induces a contrasted black and white image of the fre-surface. It increases the sensitivity to deviations from a perfect paraboloid.

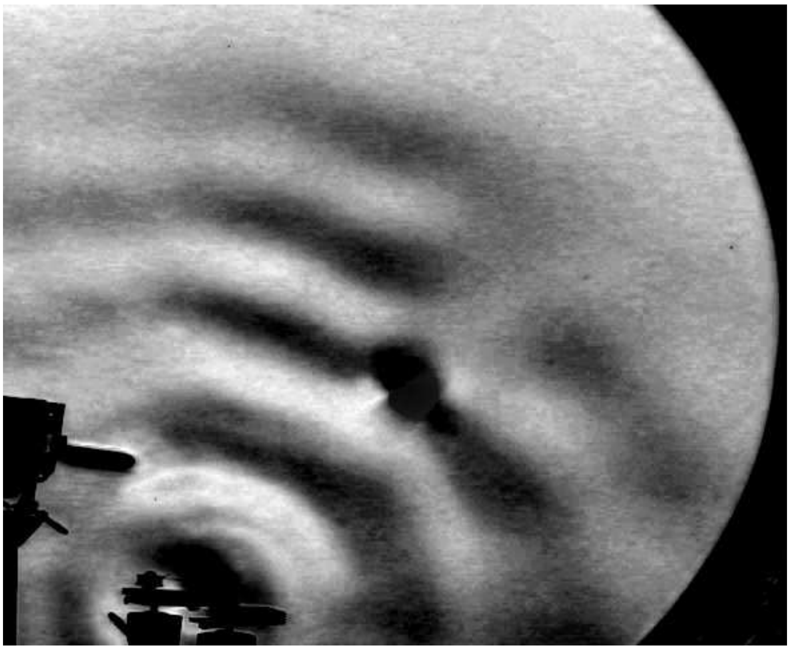

FIGURE 11 Optical altimetry visualisation of inertia-gravity waves ($50\mu m$ in amplitude) interacting with a localized vortices. The wave maker is on the bottom left, while the vortices appears in the center. Courtesy Y. Afanasiev.

Nevertheless, a quantitative method of determination of the slope variation using speckle patterns is possible. A reference image of the fluid layer in solid-body rotation is first made. The slope is measured by comparing the original pattern and a reflected image of this pattern distorted by the surface perturbation induced by the relative flow motion. The procedure is analogous to PIV process where correlations are computed between the small areas of the image and the reference. Nevertheless, the speckle method is limited by large amplitude deformation and have a limited spatial resolution due to the minimum size of the correlation boxes (Rhines *et al.*, 2006; Afanasyev *et al.*, 2006).

A different quantitative method based on optical color coding was also developped using every pixels of the image. A color slide is fixed just below the light source. For a given rotation rate (the null point) the entire surface of water is illuminated by only one color. Any perturbation of the free surface results in the appearance of color different from the null point. It is then possible to measure from each pixel of the image the x and the y component of the slope with a 0.1% sensitvity (more details are given in (Afanasyev *et al.*, 2006)). Hence, by integrating the slope field quantitative height measurements of the parabolic fluid layer could be achieved.

Optical rotation

An over sophisticated remote sensing method for measuring the thickness of a fluid layer relies upon the optical rotation properties of the working fluid. The liquid is chosen to be optically active (limonene and CFC-113 for instance), so that plane-polarized white light propagating vertically through the fluid layer has its plane of polarization rotated by an angle which depends upon both the wavelength and the layer depth. After leaving the fluid, the angular-dispersed white light passes through a sheet of polaroid. For a given layer depth, only light of a certain wavelength has its polarization axis rotated into exact alignment with the polaroid. Light of other wavelengths is either partially or fully extinguished by the polaroid, giving a correlation between the interface height and colour registered by the camera (Hart and Kittelman, 1986; Williams *et al.*, 2004. A high-sensitivity up to $1-2\%$ of the layer height could be reached with this technique. Both the large-scale geostrophic flow and small-scale waves could be accurately measured with the technique. According to figure 12 small-scale fluctuations in the two-layer interface having 1 to 5 mm amplitude are quantitatively detected. However, the sensitivity will be optimal when the mean rotation angle is about $90°$ and this implies for the limonene/CFC mixture that the fluid layer should be relatively thick $H = 10 - 15cm$. Besides, specific precautions should be taken to prevent harmful limonene vapours from evaporating into the laboratory.

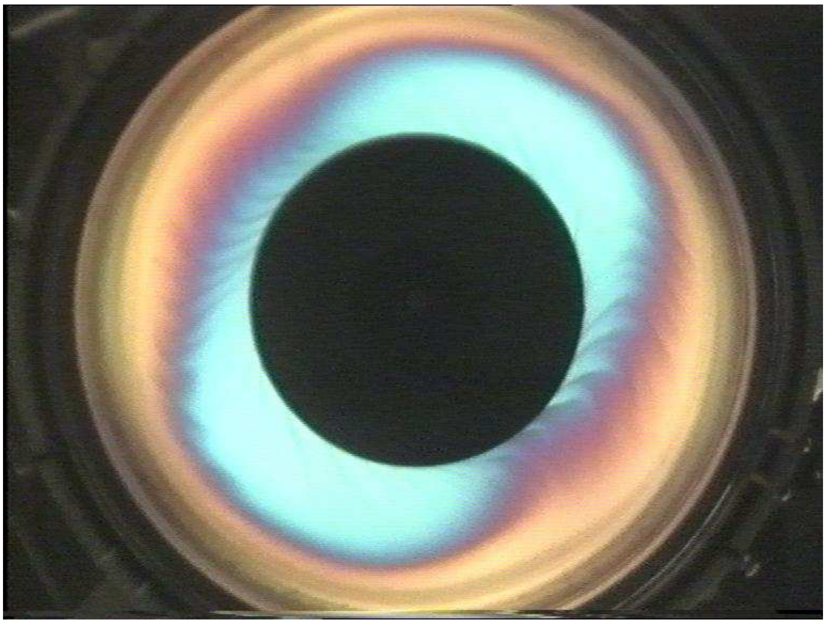

FIGURE 12 Color calibrated visualisation of the internal interface of a two-layer fluid using opticaly active CFC-13/limonene for the lower layer. Small-scale waves (5 mm amplitude and 2 cm wavelength) are visisble during one cycle of a large-scale and unstable baroclinic mode 2. Courtesy P.D. Williams.

Laser induced visualization

Laser induced visualization (LIV) technique could also be used in rotating experiments to measure with precision the fluid layer thickness along a line. Initially, the working fluid is uniformly mixed with a fluorescent dye. A vertical laser sheet crosses the horizontal fluid layer and induces the fluorescence of the dye within this plane (Figure 13 (a) and 14). In order to optimize the fluorescence, the maximum of dye absorption λ_{abs} should be close to the laser wavelength. Hence, we chose the fluoresceine ($\lambda_{abs} = 490nm$) or the Rodhamine 6G ($\lambda_{abs} = 530nm$) if we use, respectively, an argon laser ($488nm$) or Nd:Yag laser ($532nm$). A video camera, fixed on the side of the tank and perpendicular to the laser sheet could then record the fluorescence of the fluid layer. Using an adequate image processing we then detect the position of the interface between the light fluorescent and the dark transparent fluid (figure 13(b)). With this non-intrusive technique we were able, for the two-layer configuration, to measure the displacement of the fluid interface between the fresh and the dense water with an accuracy of 2% at fast acquisition rates (Stegner *et al.*, 2004; Perret *et al.*, 2006). The acquisition frequency is limited by the acquisition rate of the camera and the transfert capacity of the video card. A frequency of $100Hz$ could be easily reached nowadays with standard firewire cameras. Note in Figure 15 that the LIV camera is not exactly perpendicular to the fluid layers, in order to reduce the image distortion due to the ray diffraction through the stratified interface between the two layers

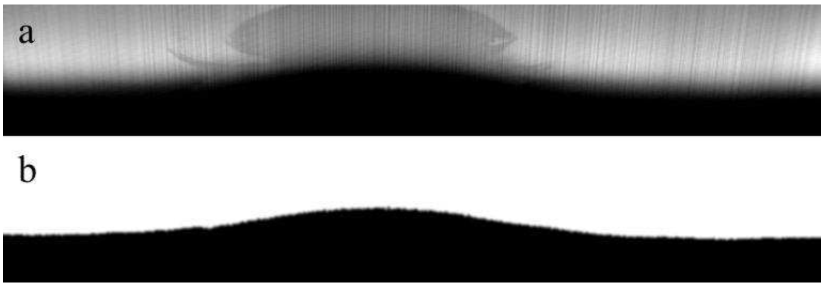

FIGURE 13 Side view visualization (a) of the fluorescent upper layer. The lower layer appears dark because it does not contain any fluorescent dye and remains therefore transparent to the laser sheet. Edge detection processing (b) allows for a precise measurement of the layer thickness corresponding here to a cyclonic depression: $Bu \simeq 0.4$, $\lambda \simeq 0.5$, $\alpha \simeq 0.75$, $\delta \simeq 0.1$.

Unlike the previous techniques which estimate the height field or its fluctuations in the whole layer, the LIV method gives a measurement of the height field only along a line. Hence, the position of the vertical laser sheet should be carefully chosen. However, this limitation is compensated by the possibility to detect small-scale and three-dimensional structures along the vertical. Indeed, this method measure precisely the dye distribution at each point (x, z) of a vertical plane and does not integrate the information along a vertical ray path. Besides, we could also measure the density field from the fluorescent dye emission (figure 14(a)). Indeed, on short time scale (i.e. few minutes) the mixing of the initial uniform concentration of both dye and salt is expected to be driven mainly by convection (i.e. turbulent mixing). Hence, dye and salt gradient are not affected by relative diffusion and they are therefore proportionnal. In a first step, we measured the relative fluorescent light emission (figure 14(b)) which depends mainly on the dye concentration and the laser sheet intensity. Then, taking into account the vertical distribution of the laser sheet intensity, we correlate the light intensity with the local salinity (i.e. density) as shown in figure 14(c). This could be, in the next futur, an efficient non-invasise technique to measure the density field in a continuously stratified fluid.

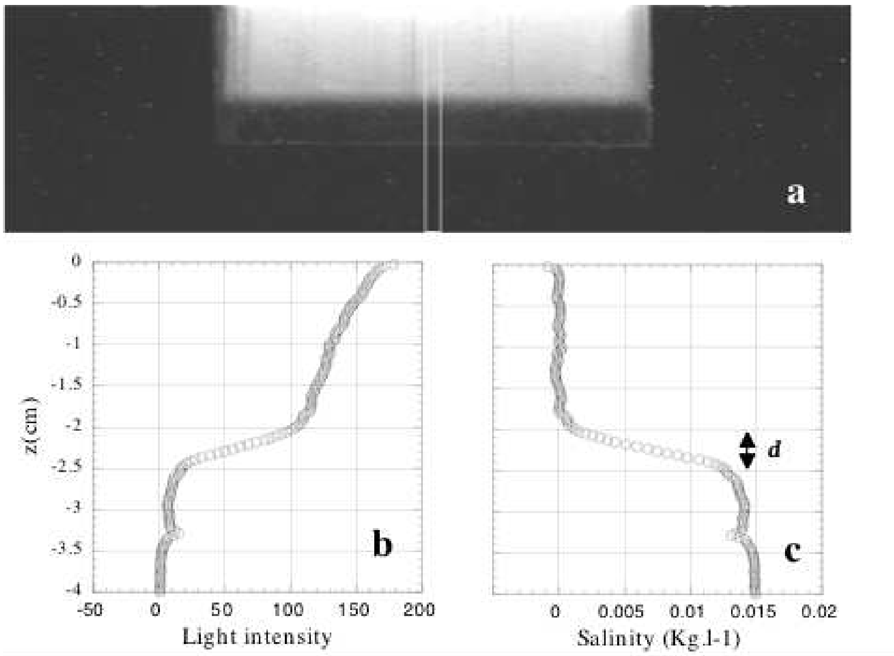

FIGURE 14 Measurement of the vertical salinity profile from the fluorescent light emission (Stegner *et al.*, 2004). Initially, the upper fluid is uniformly mixed with a fluorescent dye. (a) The upper water initially confined in a transparent bottomless cylinder appears white owing to

the fluorescent light emission while the dense water is black. (b) Vertical distribution of the light intensity in the central rectangle shown in (a). (c) The salinity profile can be deduced from (b) if we perform a careful calibration of the laser sheet intensity along the vertical plane. The disturbance at $z = -3.3$cm is due to light reflection at the bottom of the cylinder.

2.3 Potential vorticity measurements

In order to measure the potential vorticity field according to (39) we chose to use both PIV and LIV measurements simultaneously. However, due to the restrictions of the LIV technique, which gives the height field only along a line, the coupling of these non-invasive methods is best suited for unidirectional flows. It is then possible from a line measurement to estimate a global potential vorticity field for either circular (Stegner *et al.*, 2004) or parallel flows (Perret *et al.*, 2006). A typical experimental setup for a circular cyclonic PV anomaly is shown figure 15. Two lasers having different wavelengths are used in addition with specific optical filters, fixed on each camera, in order to detect the dye emission only in the vertical plane and the buoyant particles only in the horizontal plane.

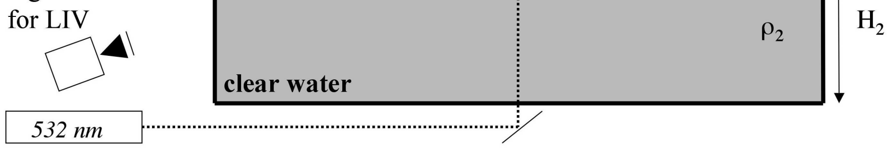

FIGURE 15 A horizontal red ($670nm$) laser sheet with a vertical green ($532nm$) laser sheet are used simultaneously in order to couple PIV and LIV measurements in the upper layer.

Time averaged vorticity and height profiles along a diameter are displayed in figure 18. Theses profiles corresponds to the PIV and LIV measurements shown in figure 8(b) and figure 13. The temporal averaging (over one inertial period $T_f = 2\pi/f$) filters out the fast wave motion from both the density interface and the azimuthal horizontal velocity. Hence, these profiles correspond to the mean adjusted state of the system which evolves slowly in comparison with the wave motion. From these data we can then easily quantify the potential vorticity (figure 16(c)) of the cyclonic PV anomaly. The PV profile is rescaled here by $Q_0 = f/H_1$, the intrinsic PV of the unperturbed upper fluid layer (solid line in figure 16(c)). For this case, the initial circular PV anomaly was a constant Q patch with $Q/Q_0 = 2$.

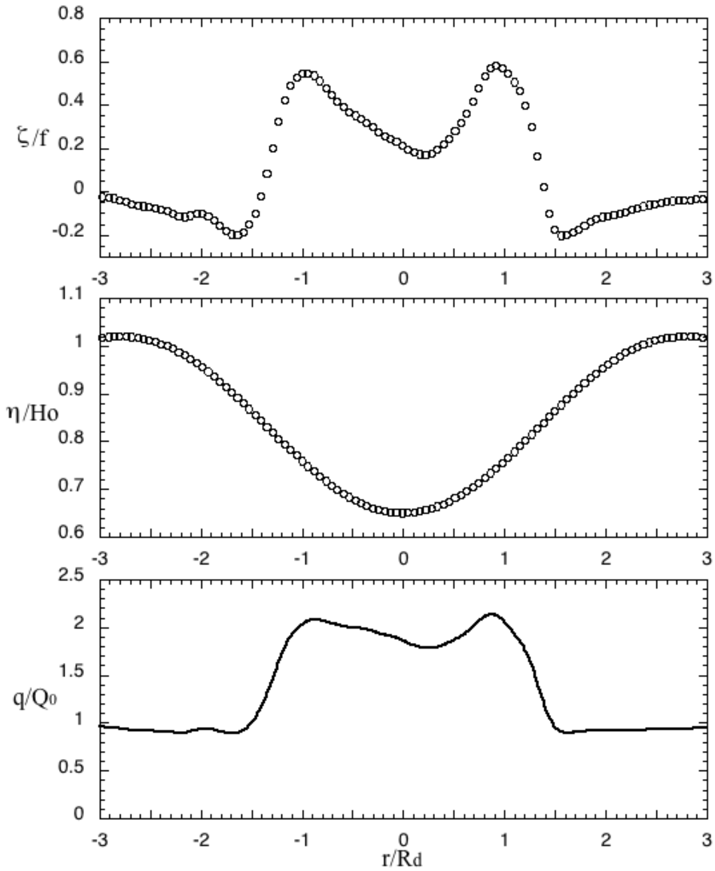

FIGURE 16 Plots of the averaged vorticity profile measured by PIV (a) and the averaged height profile (b) measured by LIV corresponding to the mean steady state at $t = 2T_f$. The potential vorticity (c) is deduced from these two profiles. These measurements correspond to the same cyclonic PV anomaly shown in figures 8(b) and 13.

As far as we know, this technique is the first attempt for direct and quantitative measurements of the potential vorticity field in a rotating shallow-water layer experiment. In other laboratory studies, either the height field or the velocity field were measured but not both of them simultaneously. In such case, the “missing” field could be estimated according to the geostrophic or cyclo-geostrophic balance and the potential vorticity field reconstructed. Nevertheless, these indirect methods could induce significant errors especially when ageostrophic or non-hydrostatic motions become non negligible. A more refined method based on data assimilation was used recently (Thivolle-Cazat *et al.*, 2005). The experimental results were compared with a two-layer isopycnal model and data assimilation was used to extrapolate from PIV measurments both the interface position and the potential vorticity field. However, such PV extrapolation depends strongly on the underlying assumptions of the numerical model used and on the assimilation scheme. Therefore, we do believe that coupled measurements is the best way to quantify the PV. Nevertheless, data assimilation will fully benefit from these coupled measurements and it could become an optimal method to test the limits of validity of the shallow-water modelisation for real flows.

3 Simple case studies of geostrophic adjustment

We describe in what follows few cases of geostrophic adjustment based on lock released experiments performed in rotating fluids. In a two-layer configuration, vertical boundaries (i.e. locks) are used to fix initial height (or density) steps in the upper layer. For such cases when there is no relative motion in the layers the initial PV field is precisely controlled by the layer thickness. If the release of the vertical walls is rapid enough, we could then follow the geostrophic adjustment of a well defined initial condition corresponding to discontinuous profiles of constant PV. The simplicity of the initial condition makes these experiments easily reproducible.

3.1 "Warm-core" lens

Initial state and experimental configuration

The term warm-core lens is generally used for mesoscale vortices which contain a finite volume of warm and light water at the ocean surface. A simple experimental configuration leads to similar dynamical structure (Griffiths and Linden, 1991; Rubino and Brandt, 2003). A fixed volume of buoyant water is initially confined within a bottomless cylinder of radius R_c on the top of a dense rotating fluid (figure 17 (a)). Assuming that the thin upper layer follows the reduced-gravity RSW equations (c.f. Chapter 1), the initial PV distribution is constant for $r < R_c$ and exhibit a singularity at $r = R_c$ (figure 17 (b)) due to the vanishing layer thickness. Similar experiments were performed to study the baroclinic instability of a density front leading to meanders and eddies (Griffith and Linden, 1991; Bouruet-Aubertot and Linden, 2002). The present experiment was made with a smaller thickness ratio parameter $\delta \simeq 0.1$ to reduce the growth rate of baroclinic disturbances and focus the study on the adjustment process (Stegner *et al.*, 2004).

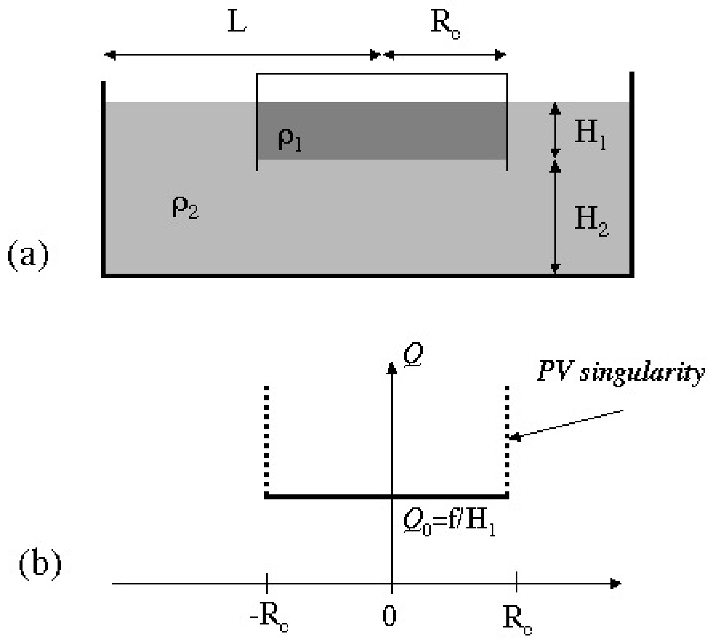

FIGURE 17 Initial configuration of the "warm-core" lens: the setup (a), and the initial profile of the corresponding potential vorticity (b).

Dynamical stages

Three stages were observed during the adjustment process. Just after the rapid withdrawal of the transparent cylinder, the fresh water spreads radially as a gravity current. During this initial stage, the flow is fully three-dimensional (figure 18 (a)) and the effects of rotation are expected to be weak. After approximately half of the inertial period, the radial extension of the lens is stopped (Ungarish and Uppert, 1998). The second stage corresponds to a radial contraction of the lens where steep jumps at the interface may appear (figure 18 (b)). Then, after about two inertial periods, the density front reaches an equilibrium characterized by a standing wave mode superimposed on the mean state (figure 18 (c), (d)). In all our experiments, this third stage is rapidly reached after approximately one or two inertial periods. These results agree with previous studies (Mahalov *et al.*, 2000) who also found that the inertial period is the characteristic time of the transition from a density current to a geostrophic front.

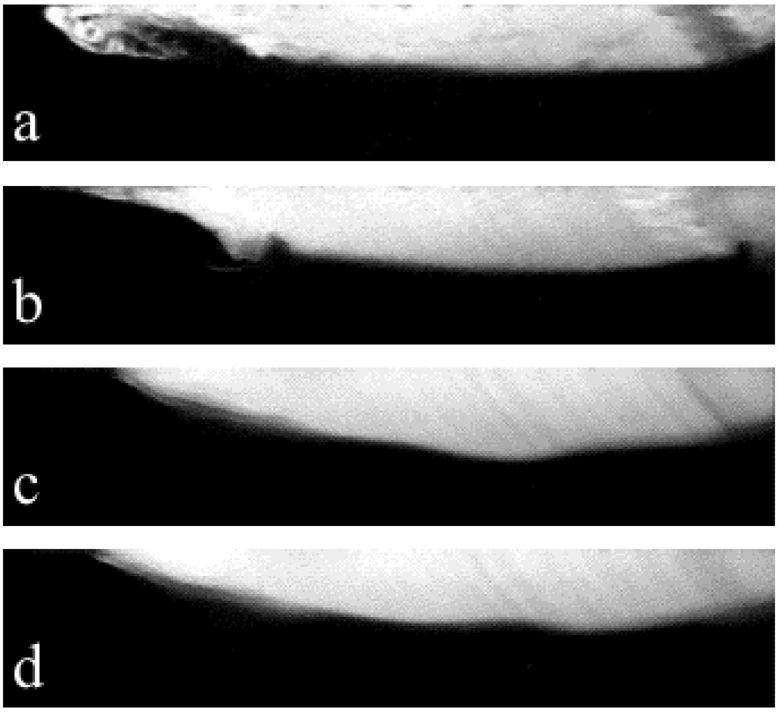

FIGURE 18 Dynamical evolution of the interface for the initial configuration corresponding to $Bu = (R_d/R_c)^2 \simeq 0.4$; $\alpha \simeq 0.76$; $\delta \simeq 0.08$ (Stegner *et al.*, 2004). The snapshots are taken at $t = 0.5T_f$ (a), $t = 0.8T_f$ (b), $t = 3T_f$ (c) and $t = 0.5T_f$ (d). The dark rays on the right hand side of the image are experimental shadows produced by the upper fixations of the cylinder.

Rotating Shallow-Water predictions

We present here the approximations and the calculation of classical Rossby adjustment theory for the axisymmetric warm-core lens configuration (figure 17). According to the small thickness ratio parameter $\delta \simeq 0.1$ and the weak motion observed in the lower layer $Ro^{(2)} \simeq \delta Ro^{(1)}$ (Stegner *et al.*, 2004) the reduced gravity RSW equations are expected to provide, in first order of approximation, an accurate description of the upper layer dynamics. Besides, we assume that viscosity and dissipative effects are negligible and that the system reaches a final steady state. Using the deformation radius as the characteristic horizontal scale (i.e. $Ro = 1$ and $\lambda = 1$) we get the following dimensionless cyclo-geostrophic balance for an axisymmetric steady state:

$$\frac{v^2}{r} + v = \partial_r \eta \tag{41}$$

The Lagrangian conservation of PV implies a constant value for all fluid parcel within the upper lens:

$$Q(r \geq r_f) = 1 = \frac{1 + \partial_r v + v/r}{1 + \eta} \tag{42}$$

where r_f is the final radius of the density lens. According to (41) and (42) we get:

$$\frac{1}{r}\partial_r(r\partial_r v) - \frac{v}{r^2} - (v + \frac{v^2}{r}) = 0 \tag{43}$$

with the boundary conditions

$$v(0) = 0 \tag{44}$$

$$h(r_f) = 1 + \eta(r_f) = 0 \Rightarrow (\partial_r v + \frac{v}{r} + 1)(r_f) = 0 \tag{45}$$

For a given radius r_f, we can solve (43), (44) and (45) numerically with standard shooting methods. Then, the angular momentum conservation or mass conservation or mass conservation both give the same implicit relation between r_f and the initial radius of the cylinder r_c:

$$r_c^2 = r_f^2 + 2r_f v(r_f) \tag{46}$$

The velocity $v(r)$ and the height $h(r)$ profiles of the steady adjusted density lens are fixed by a single parameter $r_c = R_c/R_d = Bu^{-1/2}$. Exemples of velocities and height profiles are given in figure 21 for the same initial state and two different deformation radii corresponding to $Bu = 0.05$ and $Bu = 5$. For small Burger number we expect an axisymmetric jet (or large-scale ring) whereas for large Burgers number an eddy (close to solid rotation) is expected.

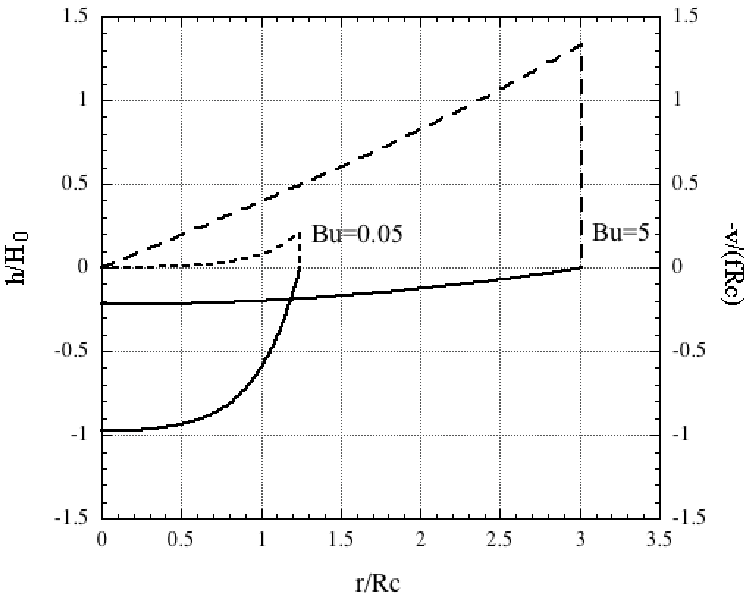

FIGURE 19 Final steady state according to the standard Rossby adjustment. Two adjusted velocity (dashed line) and height (solid line) profiles resulting from the same initial density anomaly ($h = H_1$, $r = R_c$) are plotted for two different deformation radii $Bu = 0.05$ and $Bu = 5$.

Mean adjusted state

In the warm-core lens configuration, the interface between the two fluids intersects the free surface. Hence, unlike the standard Rossby adjustment problem (Gill, 1982; Vallis, 2006) inertia-gravity waves cannot propagate away from the region of the initial density anomaly. Therefore, the separation between the adjusted state and the wave motion is not direct. Hence, we used time averaging over one or two T_f, as decribed in the previous section (§ 2), in order to extract the slow dynamics of the height profile and the velocity field. We first observe that the averaged height profile, displayed in figure 20(a), remain almost constant between $t \simeq 1.5T_f$ and $t \simeq 7T_f$. During that time, the averaged velocity profile experiences a slow dissipation (figure 20(b)). Therefore, even if a strong wave activity is present according to figure 18, the averaged mean state remains quasi-steady after one or two inertial periods. Moreover, in the central region, this quasi-steady state is relatively close to the cyclo-geostrophic adjusted state predicted by the PV conservation in the RSW framework. According to this inviscid ajustment model the velocity reaches its maximum and is discontinuous at the edge of the lens. This is obviously unrealistic in a physical system where dissipative processes occur. Indeed, according to figure 20(b) the maximum velocity is almost three times smaller than the predicted one. Hence, both the velocity and the potential vorticity of these anticyclonic lenses are smoothed near the edge front over a characteristic distance equal to the deformation radius (in the present case $R_d = 3.2cm$ while $R_c = 5.25cm$).

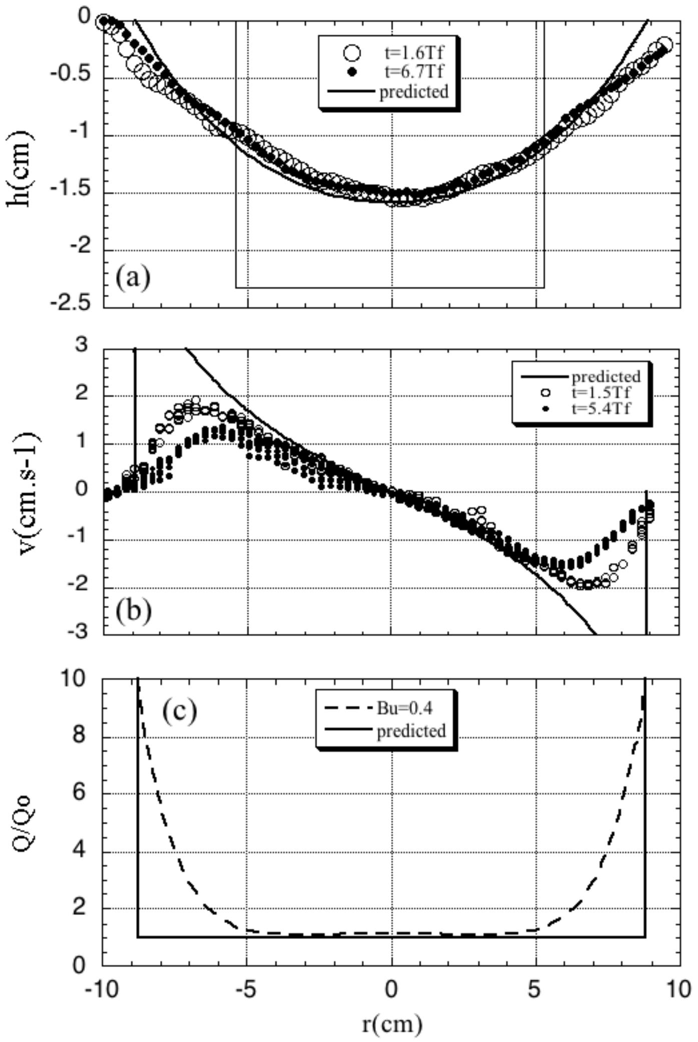

FIGURE 20 Mean height (a), velocity (b) and PV (c) profiles averaged over one inertial period. The initial density anomaly confined within the bottomless cylinder is plotted with a thin line in (a). The thick solid line corresponds to the cyclo-geostrophic adjusted state predicted by the geostrophic adjustment scenario of the inviscid RSW model.

Small-scale instabilities

Detailed analysis of the velocity field evolution show that strong and localized dissipation occurs in the very initial stage of adjustment ($t \leq 2T_f$) while the flow experiences only a weak dissipation afterwards. This rapid dissipation which occurs at the edge of the anticyclonic lenses induces a significant deficit in the kinetic energy of the adjusted flow up to 50% or 80% (Stegner *et al.*, 2004). Dye visualization reveals that transient and rapid three dimensional instabilities occur in the very first stage of adjustement (figure 21). A first unstable perturbation having a short wavelength grows very quickly, then spiralling arms appear with a larger wavelength. The first instability scales with the viscous diffusion length $L_v = \sqrt{\nu T_f} \simeq 3 - 4mm$ and does not depend on the Burger number while the secondary mode corresponding to the spiralling arms does scale with the deformation radius. These three-dimensional instabilities localized in time (less than one inertial period) and space (the edge of the anticyclonic lens) provide an efficient mechanism of turbulent dissipation which cascades energy toward small scales in the frontal region. However, outside the outcropping region the potential vorticity conservation is well verified.

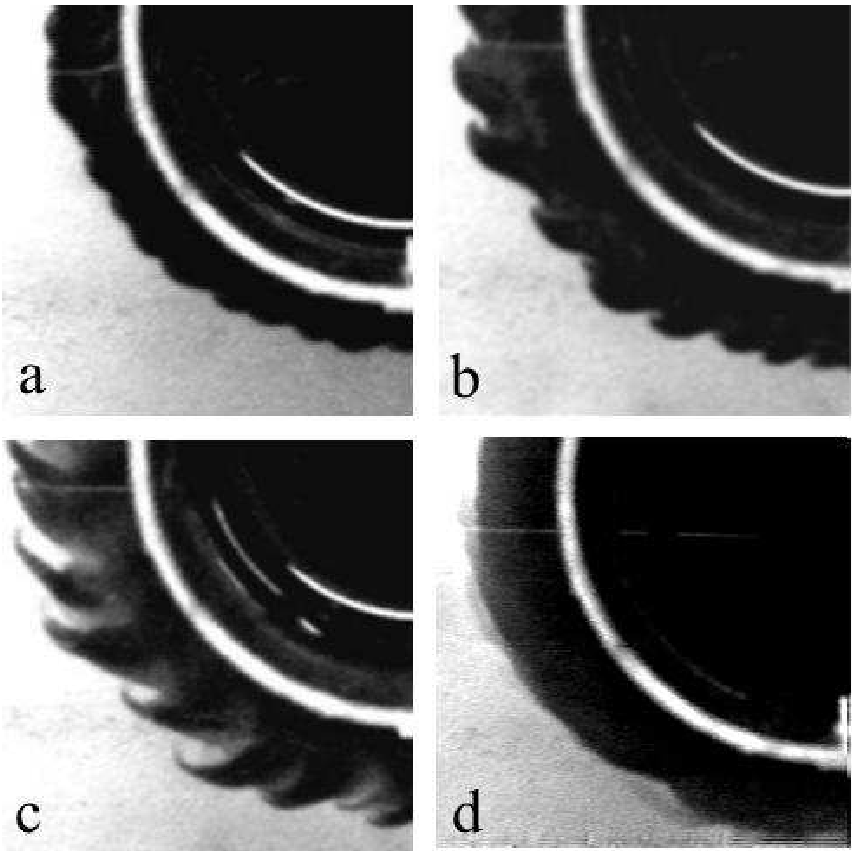

FIGURE 21 Dye visualization of the three-dimensional perturbations at the edge of the anticyclonic lens (a) $t = 0.3T_f$, (b) $t = 0.5T_f$, (c) $t = 0.7T_f$ and (d) $t = 1.7T_f$ (Stegner *et al.*, 2004).

3.2 Cyclonic and anticyclonic PV patches

Initial state and experimental configuration

We used the term "PV patches" for localised positive or negative potential vorticity anomalies of constant values within a uniform PV layer. The "PV patch" model is the generalisation of the Rankine vortex (cylindrical vorticity patch) for a rotating shallow-water layer. It is the simpliest description of potential vorticity front with no outcropping. It could be, for instance, a simplified description of the cyclonic polar vortex in the stratosphere. The corresponding experimental configurations for anticyclonic and cyclonic "PV patches" are shown respectively in figure 23 (a) and figure 23 (b). A two-layer stratification with a small thickness parameter $\delta = 0.125$ is first realized. Then, a bottomless cylinder is used to produced an height step in the two-layer interface. Assuming that the thin upper layer follows the reduced-gravity RSW equations, the initial PV distribution is uniform inside ($r < R_c$) and outside ($r > R_c$) the cylinder. Unlike, the "warm core" lens configuration (figure 17) the potential vorticity exhibit a discontinuity (but not a singularity) at $r = R_c$ due to the finite jump in the layer thickness. Besides, both positive and negative circular PV jumps could be obtain (figure 23 (b), (c)). A positive (negative) thickness anomaly in the upper layer correspond to a negative (positive) PV jump and will generally lead to a localized anticyclonic (cyclonic) circular ring or vortex.

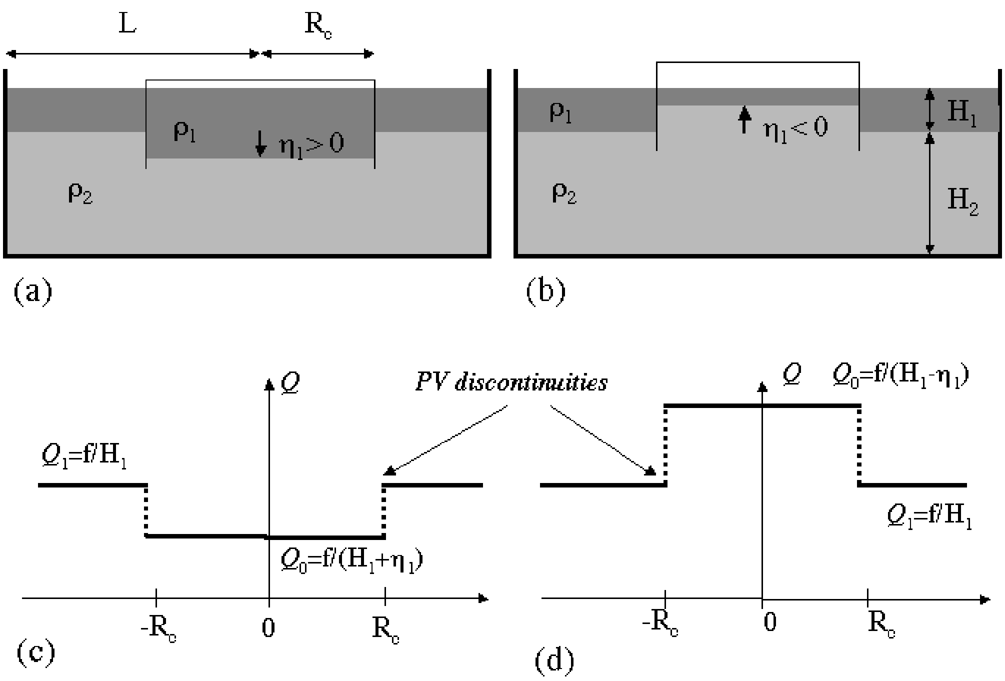

FIGURE 22 Initial configuration of the experimental setup corresponding to an anticyclonic (a) and a cyclonic (b) PV patch and their respective PV profiles (c) and (d).

Dynamical stages

The very initial stage of adjustment differs from the warm-core lens configuration. Just after the withdrawal of the transparent cylinder, the vertical density jump get tilted and a local overturning motion is initiated at the initial position of the cylindrical wall. However, due to the rotation, the overturning motion is stopped after one inertial period and a localized shock (steep density front) occurs as shown in figure 23 (b) and figure 24 (b). Due to the absence of outcropping front no gravity current head is visible for the PV-patch configuration. Afterwards, the thickness anomaly reaches an equilibrium. Even if, small fluctuations could be detected this mean adjusted state holds for a relatively long time. According to figures 23 (c)-(e) and figure 24 (c)-(e), for a small Burger number configuration (here $Bu = 0.084$) the amplitude and size of the mean adjusted state remain close to the initial unbalanced height profile. Besides, the thickness anomaly remain almost unchanged from $t = 2T_f$ to $t = 20T_f$. Hence, the system reaches a quasi-steady state in a very short time, approximately one or two inertial periods. For higher Burger numbers, the amplitude of the fluctuations is larger and the system seems to be far from an equilibrium. However, using an accurate time averaging to filter out the fast wave motion (see below), an averaged mean state is reached with the same rapidity. This characteristic time for adjustment (one or two inertial periods) does not depends on the size or the amplitude of the initial PV-patch.

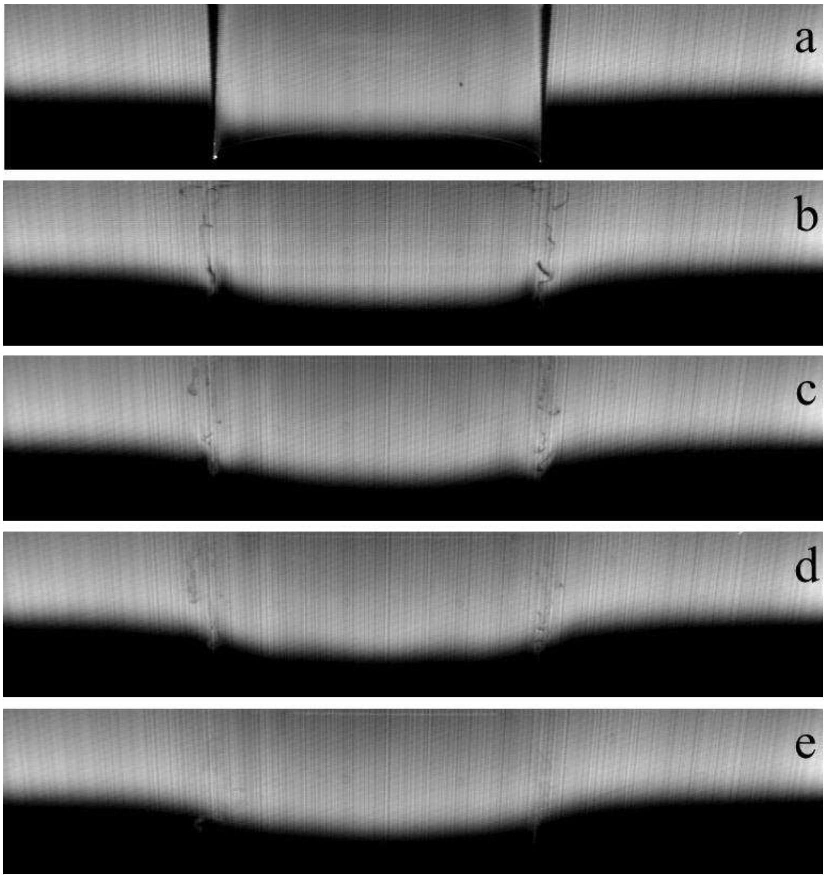

FIGURE 23 Dynamical evolution of the interface of an anticyclonic PV patch corresponding to $Bu = (R_d/R_c)^2 \simeq 0.084$; $\lambda = 0.5$; $\alpha^{(1)} \simeq 1.6$; $\delta \simeq 0.125$. The snapshots are taken at (a) $t = 0$, (b) $t = T_f$, (c) $t = 2T_f$, (d) $t = 3T_f$ and (e) $t = 10T_f$.

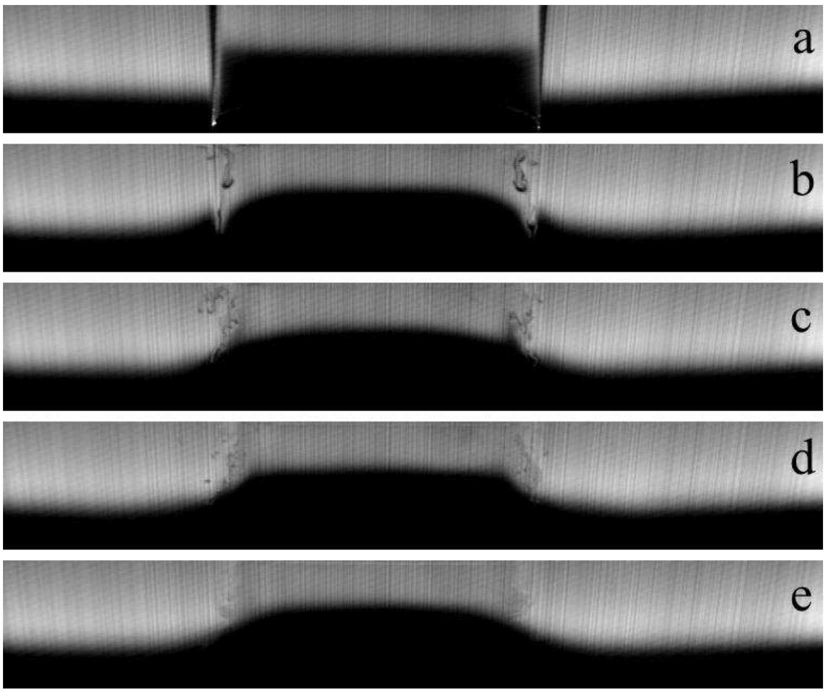

FIGURE 24 Dynamical evolution of the interface of an cyclonic PV patch corresponding to $Bu = (R_d/R_c)^2 \simeq 0.084$; $\lambda = -0.5$; $\alpha^{(1)} \simeq 1.6$; $\delta \simeq 0.125$. The snapshots are taken at (a) $t = 0$, (b) $t = T_f$, (c) $t = 2T_f$, (d) $t = 3T_f$ and and (e) $t = 10T_f$.

Rotating Shallow-Water predictions

We present here the calculation of classical Rossby adjustment theory for the cylindrical "PV-patch" configuration (figure 22). As for the "warm-core" lens case, the small thickness ratio and weak motions in the lower layer justify to use the reduced gravity RSW equations for the upper layer dynamics. Here again we neglect, at the first order of approximation, the dissipation. Therefore, we use the same set of dimensionless equations as the "warm-core" lens configuration, but we need to consider two distinct regions of uniform PV. We will use the index 0 for the inner PV anomaly region ($r < r_f$) and the index 1 for the outer region ($r > r_f$) where r_f is the radial position of the PV jump in the final adjusted state. For the case of a anticyclonic PV patch (figure 22 (c)) we expect a radial extension of the PV front ($r_c < r_f$) while for the cyclonic PV patch (figure 22 (d)) we expect a radial contraction ($r_f < r_c$) . The Lagrangian conservation of potential vorticity implies a constant but distinct value of PV for all fluid parcel within each region of the upper fluid layer. Hence, for the inner PV anomaly region we have:

$$Q_0(r < r_f) = \frac{1}{1+\lambda} = \frac{1 + \partial_r v_0 + v_0/r}{h_0} \tag{47}$$

while for the outer region we have:

$$Q_1(r > r_f) = 1 = \frac{1 + \partial_r v_1 + v_1/r}{h_1} \tag{48}$$

where the relative PV anomaly is given initially by $\lambda = \eta_1/H_1$.

Then, looking for a steady adjusted state, implies the cyclo-geostrophic balance (41) and according to (47-48) we get the second order non-linear ordinary differential equations:

$$\frac{1}{r}\partial_r(r\partial_r v_i) - \frac{v_i}{r^2} - Q_i\,(v_i + \frac{v_i^2}{r}) = 0 \tag{49}$$

with the boundary conditions:

$$v_0(0) = 0 \tag{50}$$

$$v_0(r_f) = v_1(r_f) \tag{51}$$

$$h_0(r_f) = h_1(r_f) \Rightarrow (1+\lambda)(\partial_r v_0 + \frac{v_0}{r} + 1)(r_f) = (\partial_r v_1 + \frac{v_1}{r} + 1)(r_f) \tag{52}$$

Besides, far away from the potential vorticity front ($r \gg r_f$) , a localized solution satisfy the geostrophic balance which implies to neglect the non-linear term in (49). In such case, the general solution of the linearized equation (49) is expressed through Bessel functions. The outer velocity of a localized adujsted state should then decay at infinity as a modified bessel function of the second kind

$$v_1(r \to +\infty) \propto K_1(r) \tag{53}$$

For a given radius r_f, we can solve the equations (49-53) numerically with appropriate shooting methods. Then, as for the "warm-core" lens configuration, the angular momentum conservation leads to the same implicit relation (46) between r_f and the initial position of the front r_c (i.e. the dimensionless cylinder radius). The velocity and the height profiles of the steady adjusted PV-patch are then fixed by two dimensionless parameter: $r_c = R_c/R_d = Bu^{-1/2}$ and $\lambda = \eta_1/H_1$. Exemples of velocities and height profiles for both cyclonic and anticyclonic PV patches are given figure 25. For large Burger number, in other words a small cylinder radius in comparison with the deformation radius, the adjusted state correpond to a localized vortex (figure 25 (a)). The velocity profile exhibit a core solid rotation analogous to Rankine vortices. For small Burger number (figure 25 (b)), the adjusted state correspond to a circular jet (i.e. circular velocity ring). For all these cases, the maximum velocity radius corresponds to r_f the final position of the PV jump. Unlike, the "warm-core" lens configuration, the velocity profiles for PV-patches are always continuous. Besides, in agreement with previous studies (Kuo and Polvani, 2000), the geostrophic adjustment process induce a cylone-anticyclone asymmetry. For the same amplitude of the initial potential energy fluctuation, the cyclonic structures will be here more intense than the anticyclonic ones. Indeed, according to figure 25, for the same relative amplitude of the initial thickness anomaly, the maximum velocity of cyclonic vortices ($v_{max}/(fR_d) = 0.3$ for $\lambda = -0.5$ and $r_c = 4.47$) will always be higher than the anticyclonic ones ($v_{max}/(fR_d) = -0.2$ for $\lambda = 0.5$ and $r_c = 4.47$).

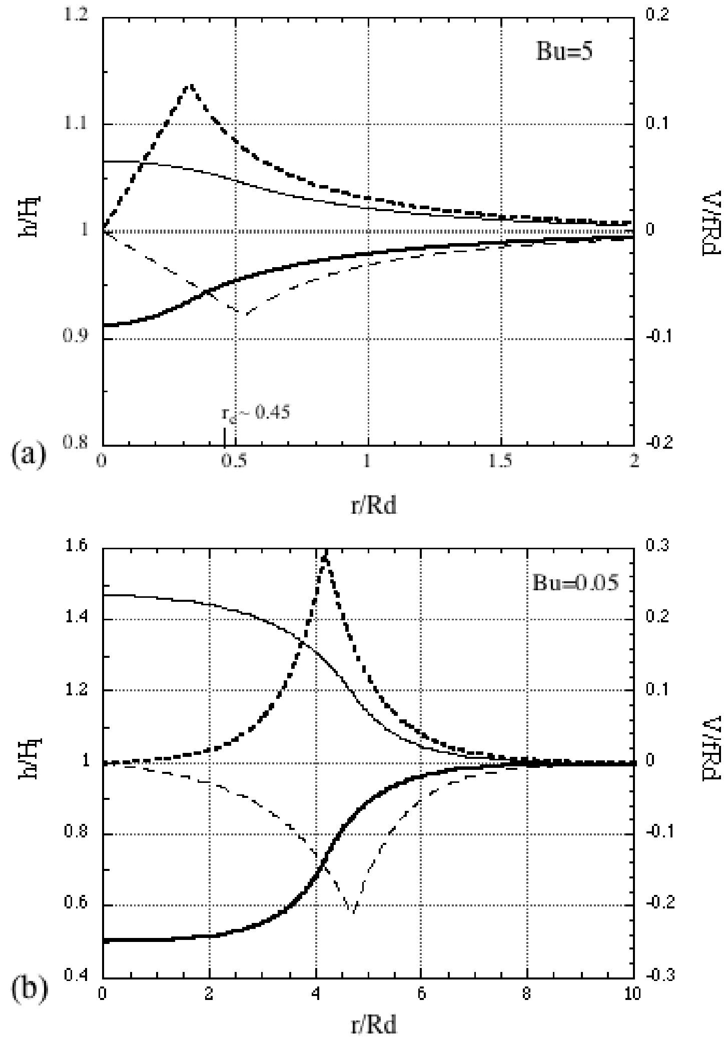

FIGURE 25 Velocity (dashed lines) and thickness profiles (solid lines) predicted by the standard geostrophic adjustment for two different sizes of the initial PV patch: $r_c = R_c/R_d \simeq 0.45$ (a) and $r_c = R_c/R_d \simeq 4.47$ (b). The anticyclonic (thin line) and the cyclonic (thick line) profiles are given respectively for $\lambda = 0.5$ and $\lambda = -0.5$.

Mean adjusted state

As for the warm-core lens configuration, we used time averaging over one or two inertial period T_f in order to extract the slow dynamics of the height profile and the velocity field. According to figure 26, we observe that both the mean height and the velocity profiles remain almost constant for several inertial periods, at least up to $20T_f$ for PV-patches having small Burger number values ($Bu = 0.083$ in figure 26). Hence, the time-averaged state have reached an equilibrium even if small wave motion could be detected both in the inner region of the PV anomaly (figure 27) and the outer region. For the cyclonic structure, the mean-adjusted state coincide perfectly with the predictions of standard geostrophic adjustment (figure 26 (a), (c)). However, for the anticyclonic structure a significant discrepancy occurs for the velocity field (figure 26(d)). The maximum velocity is at least two times smaller than the predicted one. This anticyclonic dissipation, in comparision with the non-dissipative predicted state, was observed in all the experiments from small to large Burger numbers $Bu = r_c^{-2}$. Hence, the cyclone-anticyclone asymmetry becomes even more pronouced with this unpredicted dissipation. As for the warm-core lens configuration (which corresponds to the asymptotic limit $\lambda \to +\infty$), we could suspect that this rapid dissipation of kinetic energy is due to a transient three-dimensionnal instability which affects only the anticyclonic PV fronts. However, dye visualisations appeared to be less efficient for the PV-patch experiments and we could hardly capture small-scale pertubations. We should note that an outcropping PV front (PV singularity) lead to intense velocities ($Ro \simeq 1$) in comparison with PV-step front (PV discontinuity) which induce continuous velocitiy field close to the geostrophic balance. Indeed, the Rossby number never exceed $Ro = 0.3$ in the PV-patch experiment, therefore ageostrophic motions and related instabilities are expected to be weaker than for the outcropping configuration.

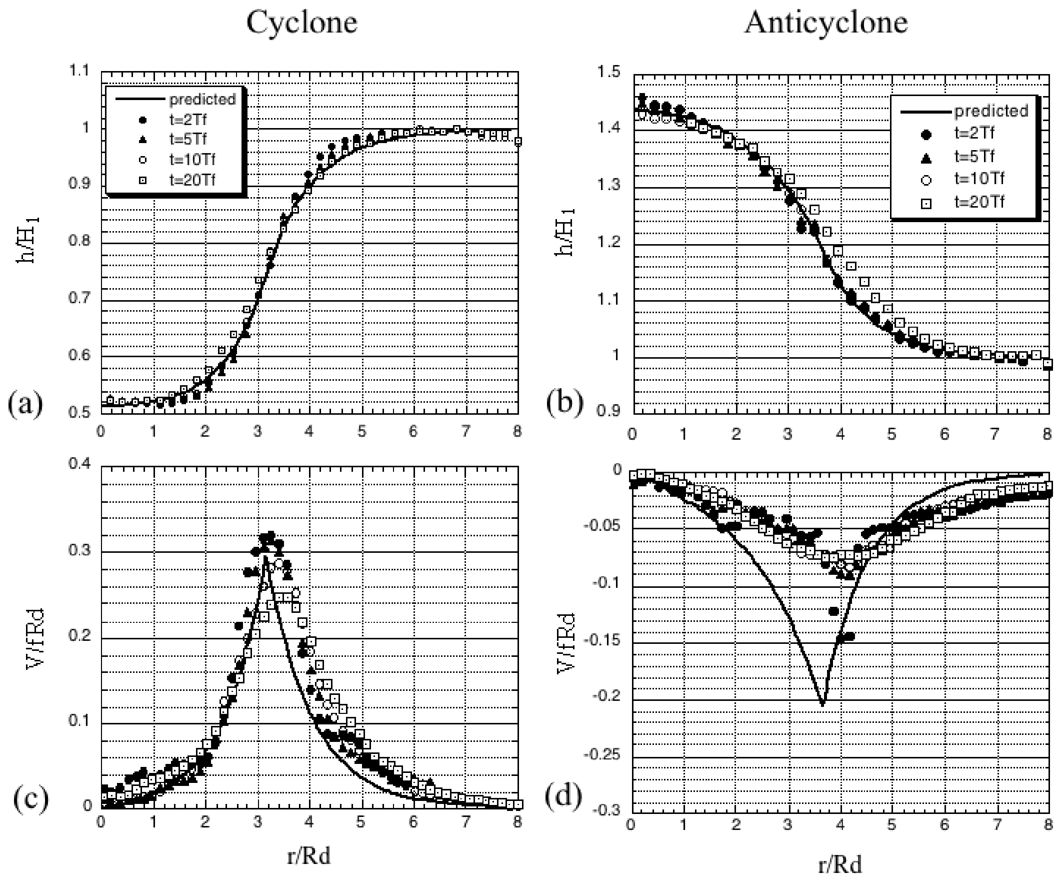

FIGURE 26 Profiles of the upper layer thickness for a cyclonic (a) and an anticyclonic (b) vortex resulting from the initial PV-patch $r_c = R_c/R_d \simeq 3.47$ ($Bu = 0.083$) and $\lambda = 0.5$ or $\lambda = -0.5$. The corresponding velocity profiles are displayed in (c) and (d). All the profiles were time-averaged over one inertial period T_f. These mean profiles are shown at various time: $t = 2T_f$ (filled circle), $t = 5T_f$ (filled triangle), $t = 10T_f$ (open circle) and $t = 20T_f$ (open square).

Inertial and sub-inertial wave activity

The geostrophic adjustment process is expected to transfert a small (large) amount of the initial potential energy to the fast wave motion for PV-patches having small (large) Burger number corresponding to $r_c = R_c/R_d > 1$ ($r_c < 1$). Hence, for the small Burger number case described above $Bu = 0.083$, the amplitude of the wave fluctuations were about few percents of the mean upper layer thickness. The sensitivity of the LIF technique was high enough to quantify this wave activity in the inner region (inside the PV anomaly) and in the outer region. Spatio-temporal diagrams (i.e. Hovmöller plots) of the wave oscillations within the cylonic and the anticyclonic PV patch are rendered figure 27. This plot shows qualitatively the temporal variations (y axis) of the upper layer thickness across a diameter (x axis). The grayscale levels were decalibrated and intensified in order to enhance the contrast for a better visualisation. Unlike the outcropping configuration, the two-layer interface extend here in the whole experimental domain and the inertia-gravity waves could freely propagate in the outer region outside the PV anomaly. Nevertheless, a significant wave activity remain for a long time (several inertial period) inside the PV anomaly even if the mean steady state is already adjusted (figure 26). A similar behavior was found in previous theoretical (Plougonwen and Zeitlin, 2005) and numerical (Kuo and Polvani, 2000) studies dealing with sharp PV fronts in the RSW dynamics.

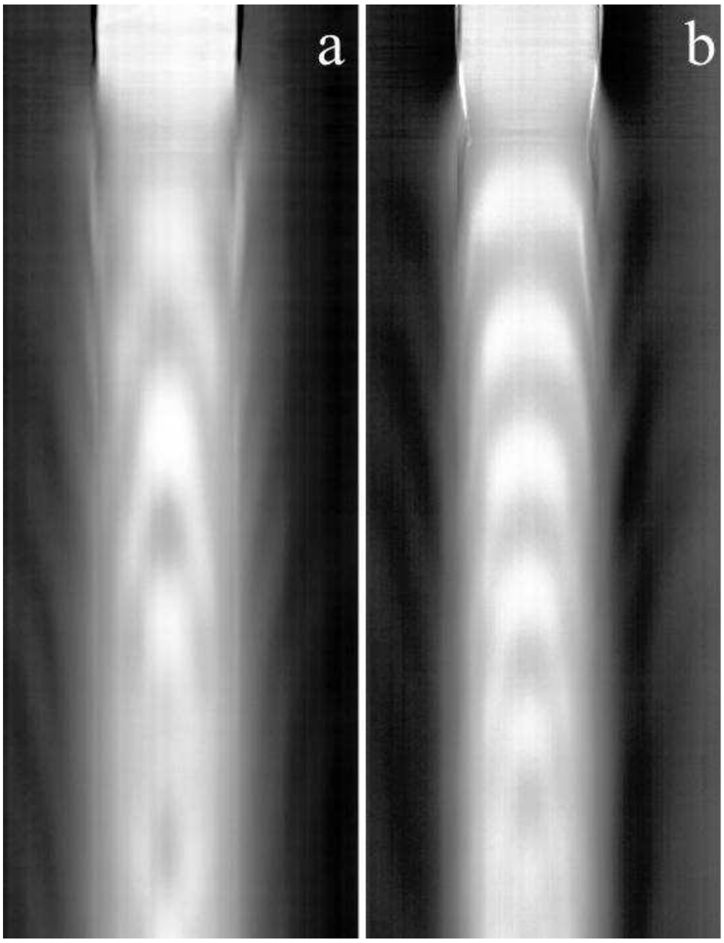

FIGURE 27 Spatio-temporal diagram of the relative fluctuations of the upper layer thickness for an anticyclonic (a) and a cyclonic (b) PV patch . The time evolve along the y axis from top ($t = 0$) to bottom ($t = 7T_f$), while the layer thickness is plotted along the x axis corresponding to a full length of 260 mm. The grayscale levels were decalibrated and intensified in order to enhance the contrast. The white rectangular area on both panels corresponds to the initial positive ($\lambda = 0.5$) or negative ($\lambda = -0.5$) height anomaly.

The most striking results is a strong cyclone-anticyclone asymmetry in the wave frequency. According to the spatio-temporal plots, the oscillation is faster for the positive PV anomaly (figure 27 (b)) in comparison with the negative PV anomaly (figure 27 (a)). Indeed, if we measure the relative fluctuations of the upper layer thickness at the center ($r = 0$), the frequency is sub-inertial ($\omega/f \simeq 0.7$) in the anticyclonic PV patch while an inertial ($\omega \simeq f$) frequency is found in the cyclonic PV patch (figure 28).

In the rotating shallow-water configuration, the apparition of sub-inertial modes ($\omega \leq f$) corresponds to trapped modes in other words, these modes must have an evanescent structure outside the PV-patch. If the relative vorticity is strong enough, a finite number of trapped modes could appear in anticyclonic vorticity region only (Kunze, 1985; Klein and Treguier, 1995; Young and BenJelloul, 1997; Llewellyn Smith, 1999; Plougonwen and Zeitlin, 2005). The present experiment shows, for the first time in laboratory, the existence of sub-inertial modes within an anticyclonic PV-patch. However, according to figure 28, these modes have a finite lifetime. Unlike, the long-lived trapped modes these sub-inertial waves probably radiate their energy to the lower layer. According to figure 28, there is no cyclone-anticyclone asymmetry in the life time of the inner wave modes. Besides, according to the spatio-temporal graph displayed in figure 27, the characteristic size of the inner wave structure, both the cyclonic (inertial) and the anticyclonic (sub-inertial) one, decays with time. This is a signature of dispersive effects, which could be induced by the high value of the wave aspect ratio $\alpha^{(2)} = H_2/L \simeq 10$ in the lower layer.

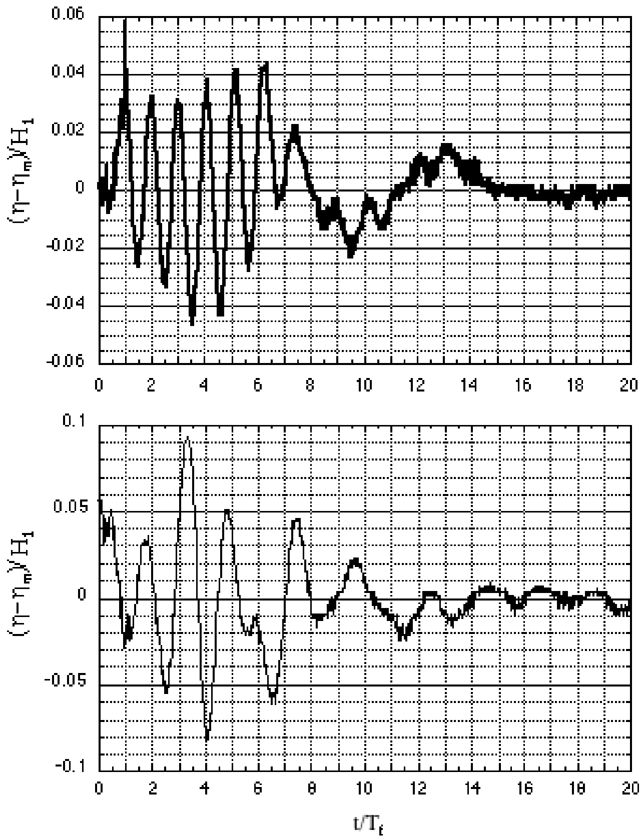

FIGURE 28 Evolution of the relative amplitude of the upper layer thickness at the center ($r = 0$) of the initial height anomaly. The case of a cyclonic (anticyclonic) PV-patch is displayed in the upper (lower) panel.

3.3 Uniform PV front

Initial state and experimental configuration

The geostrophic adjustment of a motionless horizontal density gradient generally leads to a baroclinic tilted front corresponding to a simplified model of synoptic atmospheric fronts. However, recent studies (Ou, 1984; Blumen and Wu 1995; Kalashnik 2004; Plougonwen and

Zeitlin 2005) have shown that even if the initial unbalanced state is smooth, a well defined continuous adjusted state may no longer exist. Indeed, for the case of uniform potential vorticity when the horizontal density gradient is sharp enough the steady adjusted solution exhibits discontinuities in both the density and the velocity field when the front outcropp the top or the bottom boundary.

We use a three layer setup to study the adjustment of an uniform PV front (figure 29(a)). Two upper fluid layers having different density ρ_1 and ρ_2 but the same thickness H_1 are initially separated by a bottomless cylinder. A third deep and dense lower layer acts as a neutral layer which separates the thin upper layers from the bottom boundary. According to the small thickness parameter $\delta = 0.125$ and the weak motion in the lower layer we assume that two upper layers follows the reduced-gravity RSW equations. Hence, if the upper layers have exactly the same thickness, the initial PV distribution is uniform and have the same value inside ($r < R_c$) and outside ($r > R_c$) the cylinder (figure 29(b)). However, as for the warm-core lens configuration, the PV distribution exhibit a singularity at $r = R_c$ for both the inner layer ρ_2 and the outer layer ρ_1 due to the vanishing of the layer thickness.

We can define two baroclinic deformation radius namely: $R_d = \sqrt{((\rho_2 - \rho_1)/\rho_2)gh}/f$ related to the tilted density interface between the two upper layers, $R_D = \sqrt{((\rho_3 - \rho_2)/\rho_3)gh}/f$ related to the horizontal density interface between the upper layers and one barotropic deformation radius corresponding to the dense bottom layer $R_B = \sqrt{gH}/f \simeq 1m$. The density difference between the layers ($\rho_2 - \rho_1 = 3 - 25g.l^{-1}$; $\rho_3 - \rho_2 \simeq 100g.l^{-1}$) were adjusted, in the present experiment, in order to get $R_d = 2 - 3cm \ll R_D \simeq 12cm$. Besides, the size of the rotating tank $L = 45cm$ was large enough ($L \gg R_c \geq R_d$) to neglect side wall effects. More details on the experimental procedure are given in (Mitkin *et al.* 2006).

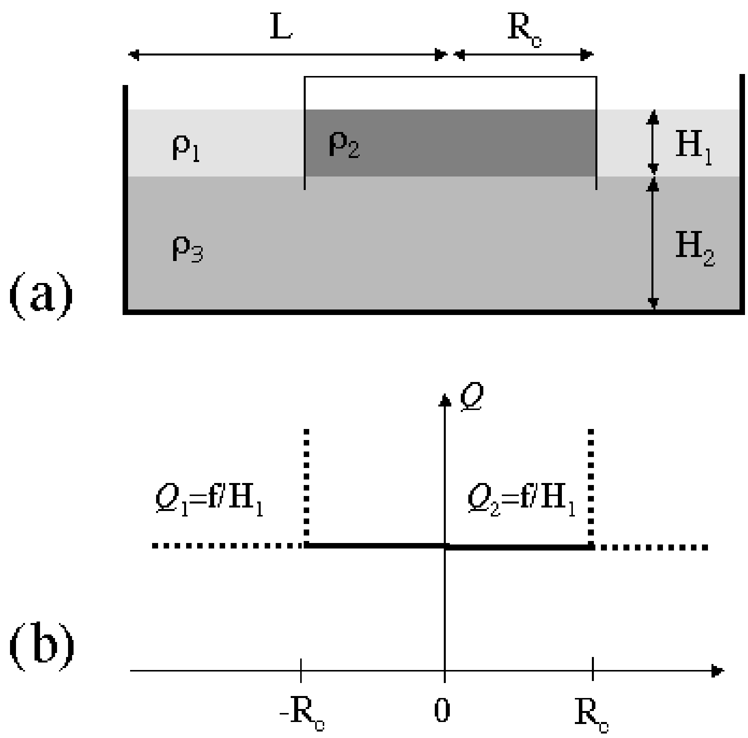

FIGURE 29 Experimental three-layer setup (a) and initial distribution of the potential vorticity (b).

Dynamical stages

Several dynamical stages were observed during the adjustment process. Just after the withdrawal of the separating cylinder, the inner dense fluid spreads radially at the bottom interface.

During this very initial stage, the flow exhibits strong three dimensional motions (figure 3*0(b)*) identical to those in a gravity current's head (Patterson *et al.* 2006). At this stage horizontal vorticity is generated at the interface between the inner and the outer upper fluid layers. After half of the inertial period the radial tilting of the density front is stopped and a reverse flow occurs. Then, in about one inertial period this tilted baroclinic front reaches an equilibrium characterized by an oscillating mean state. Theses oscillations can be seen in the fluctuations of the extremal positions r_{in} and r_{out} of the tilted front (figures 3*0(c)* and *(d)*). At longer time ($t = 5 - 10T_f$) this tilted front experiences a large-scale baroclinic instability. The initial volume of dense fluid looses its axial symmetry and splits in two vortices which move away from the center of the tank. Hence, the vertical laser sheet does not capture the central cross-section of the density field any more (figure 30 (e)).

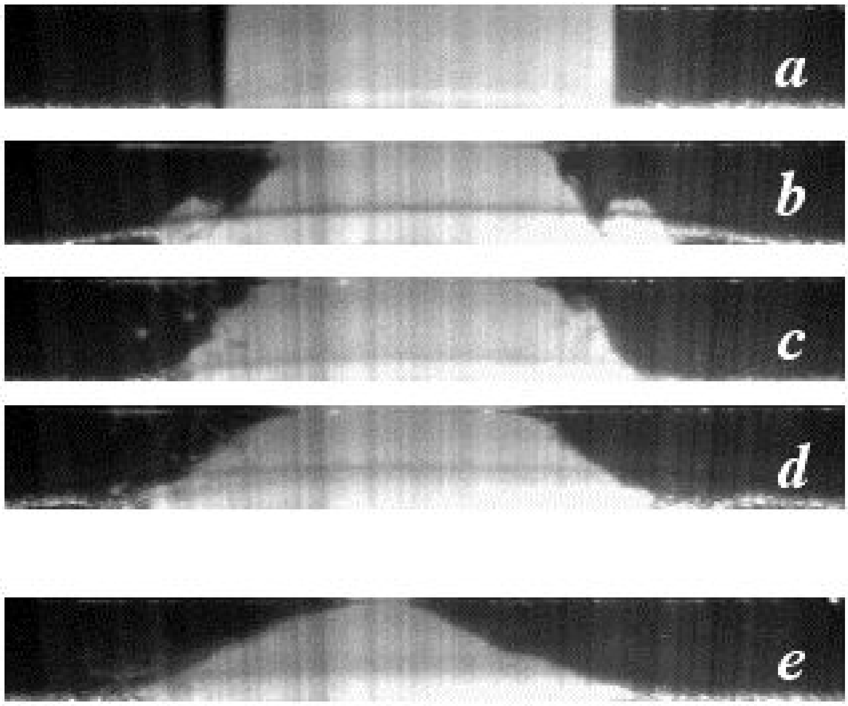

FIGURE 30 Vertical cross-section of the density front between the inner layer ρ_2 (white region) and the outer layer ρ_1 (dark region) visualized by LIV. These snapshots were taken at $t = 0$ (a), $t = 0.5T_f$(b), $t = T_f$ (c), $t = 1.5T_f$ (d) and $t = 5T_f$ (e) were $T_f = 2\pi/f = 5s$ is the inertial period. This experiment corresponds to $r_c = R_c/R_d = 2.1$ ($Bu = 0.22$; $\alpha = 1$).

Rotating Shallow-Water predictions

We assume here that: viscosity and dissipative effects are negligible ($Re \gg 1$, $E_k \ll 1$); each layer follows the rotating shallow-water dynamics ($\alpha \ll 1$) ; top and bottom boundary conditions are free-slip and rigid lid ($\delta \ll 1$, $Bu^* \gg 1$). Under these assumptions, the geostrophic adjustement of the density front is now controlled by a single parameter, namely the Burger number Bu.

We look here for an axisymmetric steady state, solution of the RSW equations in both the light outer layer 1 and the dense inner layer 2. For simplicity, we neglect the cyclostrophic terms in the horizontal momentum equations. Such approximation is valid when $R_c \gg R_d$. In this case, the steady state satisfies an exact geostrophic balance and therefore using the pressure continuity at the interface we get

$$v_1 - v_2 = \partial_r \eta \quad (54)$$

where η is the dimensionless thickness of the inner layer 2. The Lagrangian PV conservation leads to a constant PV value for all fluid parcels in both layers :

$$Q_1(r \geq r_{in}) = \frac{1+\zeta_1}{1-\eta} = 1 \tag{55}$$

$$Q_2(r \leq r_{out}) = \frac{1+\zeta_2}{\eta} = 1 \tag{56}$$

where $\zeta_i = \frac{1}{r}\partial_r(rv_i)$ is the relative vorticity and r_{in} (r_{out}) is the position of the upper (lower) intersection of the tilted density front with the top (bottom) boundary (figure 31(b)). Note that, the boundary conditions $\eta(r_{in}) = 1$ and $\eta(r_{out}) = 0$ imply a singularity in the PV field at the ends of both layers, even if the PV have the same constant value within the layers. Such singularities will be the source of discontinuities in the vorticiy and velocity field of the adjusted state (figure 31(b) and (c)). Then, the angular momentum conservation or the mass conservation gives both the same implicit relations between (r_{in}, r_{out}) and the initial radius of the density front $r_c = R_c/R_d = Bu^{-1/2}$:

$$r_c^2 = r_{in}^2 + 2r_{in}v_1(r_{in}) = r_{out}^2 + 2r_{out}v_2(r_{out}) \tag{57}$$

Besides, outside of the region of the tilted front ($r \leq r_{in}$ and $r \geq r_{out}$) there is no radial displacement of fluid parcels. Therefore, the angular momentum conservation implies:

$$v_2(r \leq r_{in}) = v_1(r \geq r_{out}) = 0 \tag{58}$$

Then, according to equations (54), (55) and (56) we obtain the following system of linear equations:

$$\partial_{r^2}\phi + \frac{1}{r}\partial_r\phi - (2 + \frac{1}{r^2})\phi = 0 \tag{59}$$

$$\partial_r(r\psi) = -r \tag{60}$$

where according to (57) and (58) $\phi(r) = v_1 - v_2$ satifies the following boundary conditions

$$\phi(r_{in}) = \frac{1}{2}(r_{in} - \frac{r_c^2}{r_{in}}) \quad ; \quad \phi(r_{out}) = \frac{1}{2}(\frac{r_c^2}{r_{out}} - r_{out}) \tag{61}$$

and

$$\psi(r) = v_1(r) + v_2(r) = \frac{1}{2}(\frac{r_c^2}{r} - r) \tag{62}$$

For a given initial radius $r_c = Bu^{-1/2}$ we can solve numerically (59) with (61) using a standard shooting method. An exemple of height, velocity and vorticity profiles in both layers are given in figure 33 corresponding to $r_c = 3.33$ ($Bu = 0.09$). Due to the volume conservation in cylindrical geometry, the front displacement in the outer layer ($r_c - r_{in}$) is not identical to the front displacement in the inner layer ($r_{out} - r_c$). This leads to higher velocity amplitude in the outer layer (figure 31(b)) according to (57). Even if the velocity field is strongly baroclinic (opposit direction in the upper and the lower layer) the vorticity is anticyclonic in both layers (figure *31(c)*) and reaches the extreme value $\zeta = -f$ at both ends of the tilted density front.

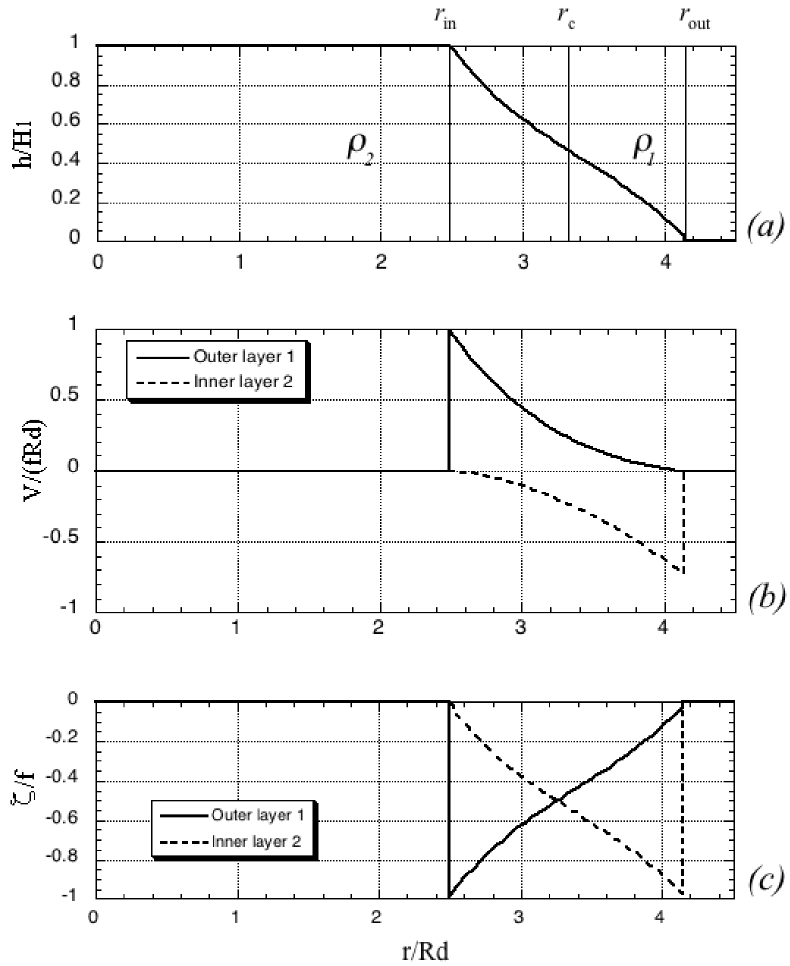

FIGURE 31 Density front (a), velocity (b) and vorticity (c) fields in the inner and outer layers of the adjusted steady-state according to the Rossby adjustment theory when $r_c = 3.33$ ($Bu = 0.09$).

Mean adjusted state

As for the previous cases, we use a time averaging over one inertial period, in order to separate the slow dynamics of the mean front and the fast dynamics of the oscillations. This temporal averaging filters out the fast dynamics on both the density front and the azimuthal velocity field.

According to figure 32 the qualitative structure of the mean adjusted state measured in the experiment is in correct agreement with the geostrophic adjustment predicted by a simple two-layer RSW model. The averaged velocity profile, measured close to the upper free surface, is displayed in figure 32(b). According to the standard inviscid adjustment model (solid line) the velocity is expected to be discontinuous in the outer layer at the upper edge of the front. This is obviously unrealistic in a physical system where dissipative processes occur. Hence, during the adjustement process a strong but continuous cyclonic shear is formed instead of the discontinuous velocity jump predicted by the inviscid theory. The width of this cyclonic shear is much smaller than the deformation radius ($0.2 - 0.3\,R_d$). Besides, the vorticity in such thin shear layer exceeds the planetary vorticity ($\zeta = 3 - 4\,f$ in figure 32*(b)*) and may induce fast small-scale instabilities. However, the spatio-temporal resolution of the particle image velocimetry we used could hardly capture such small-scale instability patterns.

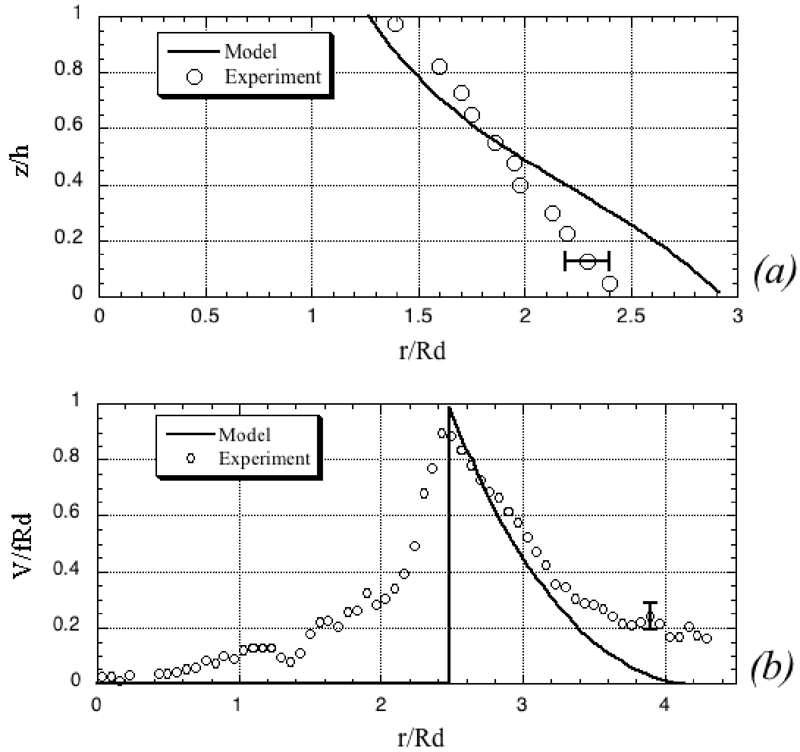

FIGURE 32 Comparison between the mean experimental adjusted state (dots) and the Rossby adjustment model (solid line). The vertical cross-section of the density profile (a) corresponds to $R_c/R_d = 2.1$ $(Bu = 0.22)$ while the horizontal azimuthal velocity (b) measured close to the upper free surface corresponds to $R_c/R_d = 3.33$ $(Bu = 0.09)$.

Small-scale instabilities

By means of LIV, we could visualize an horizontal cross-section of the sharp density gradient just below the free surface. The dynamical evolution of this sharp gradient is shown in figure 33. After the release of the bottomless cylinder the upper front experiences a rapid radial contraction. Due to the angular momentum conservation, this radial contraction generates at the same time a strong azimuthal flow. During this very initial stage, small distrubances appears at the edge of the front. Using an edge detection image processing we could accurately measure the initial wavelength λ of this instability (figure 33*(b)*). Due to its rapid growth rate this instability is probably not affected by the rotation and the wavelength of the small-scale perturbations does not depend on the deformation radius (Mitkin *et al.* 2006).

In the present case, unlike the outcropping lense configuration, no secondary instability occurs and the non-linear saturation of the initial perturbation leads to the formation of strong cusps and small cyclones appear according to figure 33*(c)*. Here again the size of theses intense cyclones could be much smaller that the deformation radius and remain independant from this latter. Theses cat eye patterns look like a classical horizontal shear instability. Nevertheless, due to the baroclinic structure of the flow, the vertical extension of these small cyclones is limited and they should be formed preferentially at the top or the bottom edge of the density front. Besides, these vortices are transient features of the adjustment process. Indeed, after half an inertial period the front reaches his maximal contraction and the small cyclones disappear during the reverse oscillation (figure 33*(d)*).

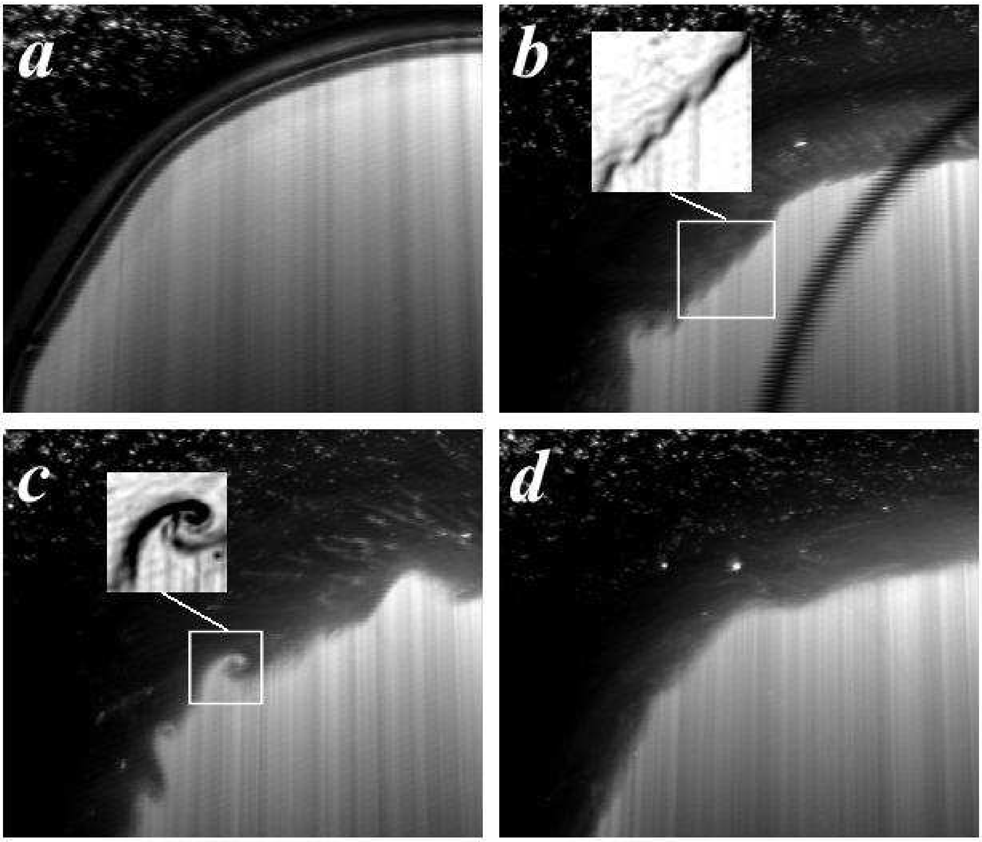

FIGURE 33 Visualization of small-scale disturbances at $t = 0$ (a), $t = 0.25T_f$(b), $t = 0.5T_f$(c) and $t = 0.75T_f$(d) in an horizontal cross-section of the density front ($Bu = 0.09$) just bellow the upper free surface. Local image processing of edge front detection are shown in (b) and (c), the black pixels corresponds to high values of the intensity gradient.

4 What do we learn from laboratory experiments ?

Laboratory experiments can hardly reproduce the complex thermodynamics (moisture, turbulent boudary layer convection, evaporation, air-sea fluxes...) and the wide range of dynamical regimes ($Re \gg 1$; $\delta \ll 1$) encounter in the atmophere or the ocean. However, the physical modeling of rotating shallow water flows is very useful especially for the geostrophic adjustment process, where several dynamical features occur on various temporal and spatial scales.

Previous laboratory experiments have shown that the geostrophic adjustement is a rapid process (Ungarish *et al.*, 2001; Bouruet-Aubertot and Linden, 2002; Rubino and Brandt, 2003; Thivolle-Cazat et al., 2005). But very few studies investigate the characteristic time of this process especially when strong wave activity is present. According to all the cases we studied, a mean adjusted state is reached after approximately one or two inertial period T_f. The rapidity of the geostrophic adjustment does not depends on the size or the amplitude of the initial unbalance state. The so called mean state is obtained from a simple time-averaging over T_f, in order to filter out the fast wave motion. We say that this averaged state reaches an equilibrium (i.e. get adjusted) when it's temporal evolution remain small in comparision with the characteristic wave frequency. Hence, even if a strong wave activity is present in the initial region of unbalance, the mean flow could nevertheless be adjusted. This experimental obsevation is in good agreement with the standard hypothesis of dynamical splitting between the fast ($\varepsilon \geq 1$) and the slow ($\varepsilon \ll 1$) component of motion. In the limit of small Rossby numbers, the asymptotic analysis shows that the slow component of motion doesn't feel the fast one (chapter 2). Therefore, the existence of a mean adjusted state does not depend on the presence (or not) of fast wave motion. Besides, the experimental results for both the warm-core lens configuration and the uniform PV front configuration showed that a mean adjusted state could be extracted from the wave motion with a simple time-averaging even for finite Rossby numbers. Hence, according to the whole set of experiments, the fast component of motion seems to have only a weak influence (if any) on the evolution of the mean adjusted state for a wide range of parameters ($Ro < 1,\ Bu \simeq 0.1 - 10,\ -0.5 < \lambda < 0.5$).

Theses two-layers or three-layers experiments also show that the PV conservation remain robust even if the initial state does not satisfy the assumptions of the rotating shallow-water model. Indeed, in almost all the cases, three-dimensional and non-hydrostatic motions (shocks or gravity current head) could occur in the early stage of adjustment. Nevertheless, the prediction of the RSW model based on the PV conservation gives a correct estimation of the mean adjusted state. A very good agreement is found for the cases of cyclonic PV front when there is no outcropping. However, the PV conservation could be locally broken in the case of outcropping fronts when the initial PV profile exhibit a singularity (i.e. the layer thickness vanish at a given position). In such case, all the experiments exhibit transient and three-dimensional instabilities localized around the PV singularity. These instabilities are an efficient mechanism of turbulent dissipation which rapidly cascades energy toward small scales in the frontal region. For the uniform PV front configuration, small and intense cyclones are formed in a very short time ($\sim 0.5T_f$) during the adjustement of a large scale anticyclonic front. The rapid formation of these structures, which are much smaller than the deformation radius, were not predicted by the standard scenario of adjustment and they could hardly be captured by standard numerical simulations which have limited spatial resolution. The laboratory experiment shows here a new mechanism of formation of small and intense structures within a large-scale synoptic front.

The relaxation of any unbalanced initial state in a rotating shallow-water model will always leads to the emission of Poincarré waves (away from lateral boundaries). In a real laboratory experiment, both hydrostatic and non-hydrostatic waves could be emitted at the same time and the spectral gap between the fast and the slow component of motion could then be filled. However, according to our experiments and previsous studies (Bouruet-Aubertot and Linden, 2002; Rubino and Brandt, 2003; Thivolle-Cazat et al., 2003) the energy released to the wave modes during the adjustment is mainly concentrated around the inertial frequency. A significant wave activity remain for a long time (several inertial period) inside both the cyclonic and the anticyclonic structures even if the mean steady state is already adjusted. For some specific configuration the anticyclonic structure may exhibit sub-inertial oscillations. Such wave activity is in good agreement with the RSW model predictions (chapter 2 and 3) and confirm the dynamical splitting between the fast waves and the slow adjusted motion. However, the inertia-gravity waves detected in the experiment have a dispersive behavior due to the finite value of the aspect ratio parameter α. This could explain why we didn't see any evidence of the wave breaking events predicted in the RSW framework (chapter 3). The small scale shocks we observed in the very initial stage of adjustment seems to be due to a local overturning event rather than a propagating wave leading to breaking.

Acknowledgements The work presented in this chapter was done in collaboration with V. Mitkin, P. Bouruet-Aubertot and T. Pichon which are gratefully acknowledge.

References

[1] Adrian, R. J. (2005) Twenty years of particle image velocimetry, *Experiments in Fluids*, **39**, pp 159-169.

[2] Afanasyev, Ya.D. and Peltier, W. R., (1998) Three dimensionnal instability of anticyclonic swirling flow in rotating fluid: Laboratory experiments and related theoretical predictions, *Phys. Fluids*, **10**, pp 3194.

[3] Afanasyev, Y.D., Rhines, P.B. & Lindahl, E.G. Altimetric imaging velocimetry: investigation of emission of inertial and Rossby waves by baroclinally unstable flows. *J. Fluid Mech.* submitted 2006.

[4] Blumen, W. and Wu, R. 1995 Geostrophic adjustment: frontogenesis and energy conservation. *J. Phys. Oceanogr.*, **58**, 2180-2195.

[5] Bouruet-Aubertot, P. and Linden, P.F. (2002) The influence of the coast on the dynamics of upwelling fronts. Part I: Laboratory experiments. *Dyn. Atmos. Ocean.* **36**, pp 153-173.

[6] Bracco, A., McWilliams, J.C., Murante, G., Provenzale, A. and Weiss, J.B. (2000) Revisiting freely decaying two-dimensionnal turbulence at millennial resolution, *Phys. Fluids*, **1**2, pp 2931.

[7] Carnevale, G. F., Kloosterziel, R.C. and van Heijst, G.J.F. (1991) Propagation of barotropic vortices over topography in a rotating tank. J. Fluid Mech., **233**, 119-139.

[8] Cushman-Roisin, B., Sutyrin, G.G., and Tang, B., (1992) Two-layer geostrophic dynamics. Part I: Governing equations, *J. Phys. Oceanogr.*, **22**, pp117.

[9] Fincham, A.M. and Spedding, G.R. (1997) Low cost, high-resolution DPIV for measurement of turbulent fluid flow, *Experiments in Fluids*, **23**, pp 449-462.

[10] Flor, J.B. and Eames, I. (2002) Dynamics of monopolar vortices on a topographic beta-plane, J. Fluid Mech., **456**, pp 353-376.

[11] Gill, A.E. (1982) Atmosphere Ocean Dynamics, *Academic Press*.

[12] Greenspan, G.P. (1968) The Theory of Rotating Fluids, *Cambridge University Press.*

[13] Griffiths, R. W. & Linden, P. F. 1981 The stability of vortices in a rotating, stratified fluid. *J. Fluid Mech.* **105**, 283-316.

[14] Hart, D.P. (2000) PIV errors correction, *Experiments in Fluids*, **29**, pp 13-22.

[15] Hart, J.E. and Kittelman, S. (1986) A method for measuring interfacial wave fields in the laboratory, *Geophys. Astrophys. Fluid Dyn.*, **36**, pp. 179-185.

[16] Hart, J.E. (2000) A note on nonlinear corrections to the Ekman layer pumping velocity. *Physics of Fluids*, **12**, pp 131-135.

[17] Holford, J.M. and Dalziel S.B. (1996) Measurements of layer-depth in a two-layer flow. *Appl. Scien. Res.* **56**, 191-207.

[18] Johnson, J.A. (1963) Stability of shearing motion in rotating fluid, *J. Fluid Mech.* **17**, pp 337.

[19] Kalashnik, M. V. (2004) Geostrophic adjustment and frontogenesis in a continuously stratified fluid. *Dyn. Atmos. Ocean*, **38**, 1-37.

[20] Klein, P. and Treguier, A. M. (1993) Dispersion of wind-induced inertial waves by a barotropic jet, *J. Marine Res.*, **53**, 1-22.

[21] Kuo, A. C. and Polvani, L. M. (2000) Nonlinear geostrophic adjustment, cyclone/anticyclone asymmetry, and potential vorticity rearrangement. *Phys. Fluids* **12**, 1087-1100.

[22] Kunze, E. (1985) Near-inertial wave propagating in geostrophic shear. *J. Phys. Oceanogr.*, **23**, 1897-1915.

[23] Llewellyn Smith, S. (1999) Near-inertial oscillations of a barotropic vortex trapped modes and time evolution, *J. Phys. Oceanogr.*, **29**, 747-761.

[24] Mahalov, A., Pacheco, J.R., Voropayev, S.I. *et al.* (2000) Effects of rotation on fronts of density currents. *Phys. Lett. A* **270**, pp 149-156.

[25] Masuda, A., Marubayashi, K., and Ishibashi, M. (1990) A laboratory experiment and numerical simulation of an isolated barotropic eddy in a basin with topographic β-plane. *J. Fluid Mech.*, **213**, 641-655.

[26] Mitkin, V., Stegner, A., Zeitlin, V. and Pichon, T. Generation of small-scale and intense cyclones during the geostrophic adjustment of large-scale fronts. *J. Fluid Mech.* submitted 2006.

[27] Nezlin M.V. and Snezhkin E.N. (1993) Rossby Vortices, Spiral Structure, Solitons. *Springer*.

[28] Nycander, J. (1993) The difference between monopole vortices in planetary flows and laboratory experiments. *J. Fluid Mech.* **254**, pp 561-577.

[29] Obukhov, A.M. 1949 On the question of the geostrophic wind. *Izv. Akad. Nauk SSSR. Ser. Geograph.-Geophys.* **13**, 291-306.

[30] Ou, H.W. 1984 Geostrophic adjustment: a mechanism for frontogenesis. *J. Phys. Oceangr.* **14**, 994-1000.

[31] Paterson, M.D., Simpson, J.E., Dalziel, S. B., and van Heijst, G. J. F. 2006 Vortical motion in the head of an axisymmetric gravity current, *Phys. Fluids*, **18**, 046601.

[32] Pedlosky, J. (1987) Geophysical Fluid Dynamics, *Springer*.

[33] Perret, G., Stegner, A., Farge, M. and Pichon, T. (2006) Cyclone-anticyclone asymmetry of large-scale wakes in the laboratory, *Phys. Fluids*, **18**, 036603.

[34] Plougonwen, R. and Zeitlin, V. 2005 Lagrangian approach to geostrophic adjustment of frontal anomalies in a stratified fluid, *Geophys. Astrophys. Fluid Dyn.*, **99** (2), 101-135.

[35] Reznik, G.M., Zeitlin, V. and BenJelloul, M. (2001) Nonlinear theory of geostrophic adjustment. Part I. Rotating shallow-water model, *J. Fluid Mech.*, **491**, pp 207-228.

[36] Rhines, P.B., Lindahl, E.G. and Mendez A.J. (2006) Optical Altimetry: a new method for observing rotating fluids with applications to Rossby and inertial waves on a polar β-plane, *J. Fluid Mech.*

[37] Rhines, P.B. Jets and Orography: Idealized experiments with Tip-Jets and Lighthill blocking. *J. Atmos. Sci.* submitted 2006

[38] Rubino, A. and Brandt, P (2003) Warm-core eddies studied by laboratory experiments and numerical modeling. *J. Phys. Oceanogr.* **33(2)**, pp 431-435.

[39] Rossby, C. G. 1937 On the mutual adjustment of pressure and velocity distribution in simple current systems. *Int. J. Mar. Res.* **1**, 15-28.

[40] Stegner, A. and Zeiltin, V. (1998) From quasi-geostrophic to strongly nonlinear monopolar vortices in a paraboloidal shallow-water experiment, *J. Fluid Mech.*, **356**, pp 1-24.

[41] Stegner, A. Bouruet-Aubertot, P. and Pichon T. (2004) Nonlinear adjustment of density fronts. Part 1. The Rossby scenario and the experimental reality, *J. Fluid Mech.*, **502**, pp 335-360.

[42] Stegner, A., Pichon, T. and Beunier, M. (2005) Elliptical-inertial instability of rotating Karman vortex streets, *Phys. Fluids*, **17**, 066602.

[43] Teinturier, S., Stegner, A., S. Viboud, H. Didelle, M. Ghil Inertial instability of von Karman street in a rotating shallow-water layer, *Dyn. Atmos. and Ocean* submitted 2006.

[44] Thivolle-Cazat, E. (2003) PhD Thesis, Univesite Joseph Fourier, Grenoble.

[45] Thivolle-Cazat, E., Sommeria, J. and Galmiche, M. (2005) Baroclinic instability of two-layer vortices in laboratory experiments, *J. Fluid Mech.* **544**, 69-97.

[46] Ungarish, M. and Huppert, H.E. (1998) The effect of rotation on axisymmetric gravity currents. *J. Fluid Mech.* **362**, pp 17-51.

[47] Ungarish, M., Hallworth, M. A. and Huppert, H.E. (2001) Axisymmetric gravity currents in a rotating system: Experimental and numerical investigations. *J. Fluid Mech*., **447**, 1-29.

[48] Vallis, B. (2006) Atmospheric and Oceanic Fluid Dynamics, *Cambridge Univesity Press.*

[49] van de Konijnenberg, J.A., Nielsen, A.H., Rasmussen, J.J, and Stenum, B. (1999) Shear-flow instability in a rotating fluid, *J. Fluid Mech*., **387**, pp 177-204.

[50] Yanase, S.., Flores, C., Metais, O. and Riley, J. (1993) Rotating free-shear flows. I. Linear stability analysis, *Phys. Fluids*, **5** No 11 pp 2725-2737.

[51] Young, W.R. and BenJelloul, M. (1997) Propagation of near-inertial oscillations through a geostrophic flow, *J. Marine Res.*, **55**, 735-766.

[52] Williams, P.D., Read, P.L. and Haine, T.W.N. (2004) A calibrated, non-invasive method for measuring the internal interface height field at high resolution in the rotating, two-layer annulus. *Geophys. Astrophys. Fluid Dyn*., **98**, pp 453-471.

[53] Williams, P.D., Read, P.L. and Haines, T.W.N. (2003) Spontaneous generation and impact of inertia-gravity waves in a strtified, two-layer shear flow, Geophys. Res. Lett. **30**, 22555. doi:1029/2003CL018498.

[54] Zavala Sanson, L and van Heijst, G.J.F. (2000) Nonlinear Ekman effects in rotating barotropic flows, *J. Fluid Mech.*, **412**, pp 75-91.

[55] Zeitlin, V. Reznik, G.M. and Ben Jelloul, M. (2003) Nonlinear theory of geostrophic adjustment. Part 2. Two-layer and continuously stratified primitive equations, *J. Fluid Mech.*, **491**, 207-228.